DESIGN AND ANALYSIS OF FIBER REINFORCED ELASTOMERIC ENCLOSURES WITH APPLICATION IN UPPER ARM ORTHOSIS

BY

GAURAV SINGH

THESIS

Submitted in partial fulfillment of the requirements
for the degree of Master of Science in Systems and Entrepreneurial Engineering
in the Graduate College of the
University of Illinois at Urbana-Champaign, 2016

Urbana, Illinois

Adviser:

Assistant Professor Girish Krishnan

Abstract

Fiber Reinforced Elastomeric Enclosures (FREEs) are soft pneumatic actuators that deform in a predetermined fashion upon inflation. They are constructed using a hollow elastomeric cylinder reinforced by two families of helical fibers. This thesis analyzes the deformation behavior of FREEs by formulating a simple calculus of variations problem that involves constrained maximization of the enclosed volume. The model accurately captures the deformed shape (kinematics) for FREEs with any general fiber angle orientation, and its relation with actuation pressure, material properties and applied load (kinetostatics). The accuracy of the model is verified by benchmarking with existing models for a popular McKibben Pneumatic Artificial muscle (PAM) actuator with two helically wrapped families of fibers having equal and opposite orientations. For FREEs with any general fiber orientations and other novel designs with no prior literature, the model is validated experimentally. This model is deemed to be useful in the design synthesis of fiber reinforced elastomeric actuators for any desired motion and force requirement. FREEs are soft, compliant, and have a high power to weight ratio, which makes them suitable for orthotic devices for upper extremities.

The second part of the thesis considers the design and fabrication of a soft pneumatic sleeve for arm orthosis that uses a contracting FREE is shown. The sleeve is designed to reduce wrist loads in patients that use crutches for ambulation, thereby reducing the risk of joint injury. It forms an alternate load path between the crutch and the forearm, circumventing the wrist. The constricting force generated by the sleeve on the arm is analyzed by a string model and validated with experiments.

Acknowledgments

Table of Contents

List of Figures

1. Introduction

1.1 Soft Robotics

Traditional robots are made up of rigid structures, have repeatable and precise motion, and are ubiquitous in many fields such as manufacturing and assembly. Although these robots have been highly successful in a variety of fields, there are applications such as wearable technologies and human assistive devices where traditional robots are not the most suitable option due to their low dexterity, rigid motion, and heavy components. To address these concerns, there has been a growing interest in the field of soft robotics [1], [2]. Soft robots are biologically inspired devices that are soft, compliant, and lightweight.

Soft robots require soft actuators to power their operations. Towards this, there are soft actuators called Pneumatic Artificial Muscles (PAM) [3], [4] that are inspired in operation by muscular hydrostats. PAMs are made of a hollow cylindrical hyperelastic membrane with two families of equal and opposite fibers wrapped helically around the cylinder. They are actuated pneumatically and can contract or extend based on the angles of wrapped fibers. In the next section, a more generalized class of soft pneumatic actuators of which PAMs form a subset is introduced.

1.2 Fiber Reinforced Elastomeric Enclosures (FREEs)

Fiber Reinforced Elastomeric Enclosures (FREEs) are soft pneumatic actuators similar in construction to PAMs introduced by Krishnan et al. [5] and Bishop-Moser et al. [6]. In FREEs, the two families of fibers can have any arbitrary fiber angles as shown in Figure 1-1b, whereas PAMs have equal and opposite fibers. Therefore, PAMs constitute a special case of FREEs. Due to these

1

fiber orientations, FREEs can generate contraction, extension, rotation, and a combination of these motions (see Figure 1-1).
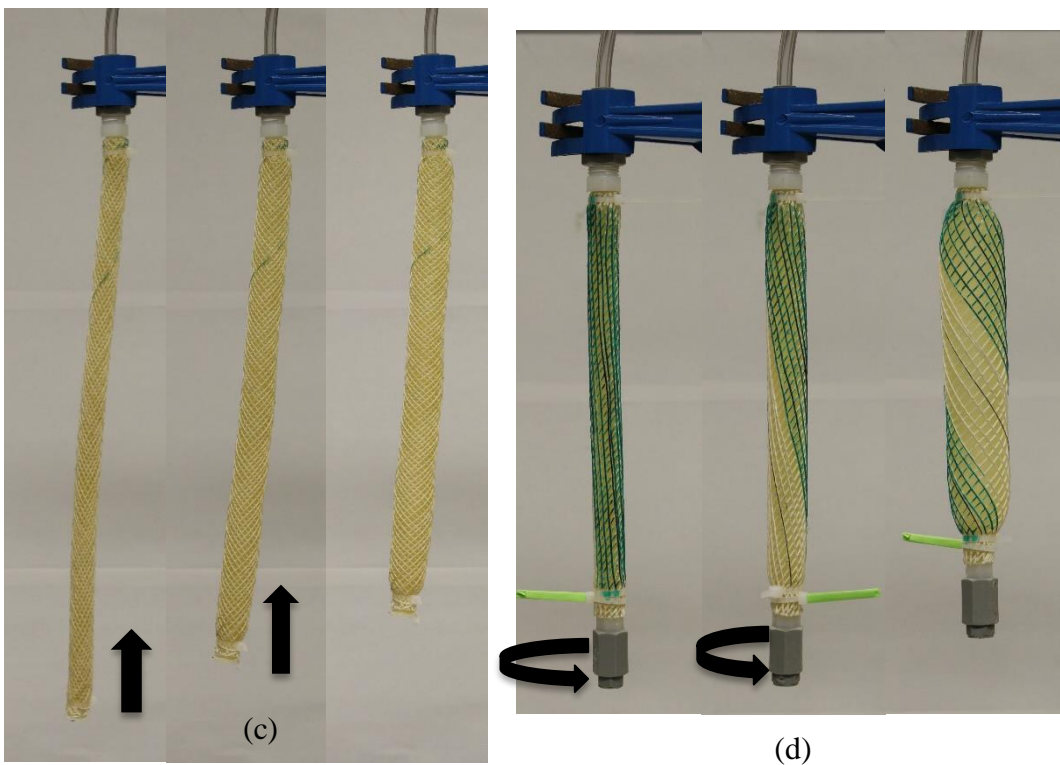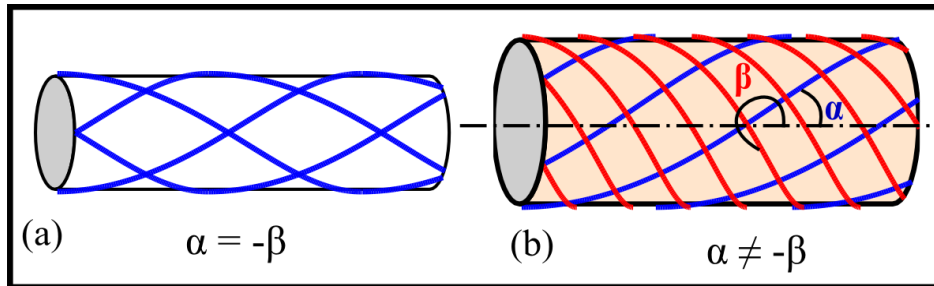
Figure 1-1 PAMs vs FREEs (a) PAMs have equal and opposite fiber orientations (b) FREEs have arbitrary fiber angle orientations that lead to different motion patterns: (c) contracting motion, and (d) rotating-contracting motion.

The design space spanned by the two fiber angles of FREEs is shown in Figure 1-2, where the antisymmetric fibers (AF) represent the design space of PAMs. Since $\alpha = -\beta$ for PAMs, only one fiber angle say α is sufficient to describe their deformation behavior. If $\alpha < 54.7°$, then upon

pressurization the PAM reduces in length (contraction) along with radial expansion. On the other hand, if $\alpha > 54.7°$, upon pressurization it increases in length (extension) accompanied with radial contraction. The blue line in Figure 1-2 is called the locked manifold (LM). The point of intersection of AF and LM is $\alpha = 54.7°$ and this corresponds to the case where PAM does not undergo any deformation upon pressurization. Krishnan et al. [5] have reported the whole span of fiber configurations which do not undergo any deformation upon pressurization. This is represented by the locked manifold in Figure 1-2.

FREEs can assume any fiber orientation shown in the two quadrants of Figure 1-2 except for the degenerate case (line DF in Figure 1-2) where $\alpha = \beta$ that corresponds to a single fiber configuration. Fiber angles shown in the regions I and II alone are unique. Fiber angles corresponding to the other regions are mirror images of I and II and therefore have the same deformation behavior. Starting at any point in regions I and II, the fiber angles converge to the locked manifold angles upon pressurization. FREEs with fiber angles corresponding to region IIa undergo rotation coupled with contraction upon pressurization, whereas the ones corresponding to IIb undergo rotation coupled with extension instead. FREEs with fiber angles in region I undergo rotation coupled with extension till the deformed angles reach the $\beta = 0°$ line beyond which it undergoes rotation coupled with contraction. Representative examples of fiber configurations corresponding to different regions on the design space is shown in Figure 1-2.
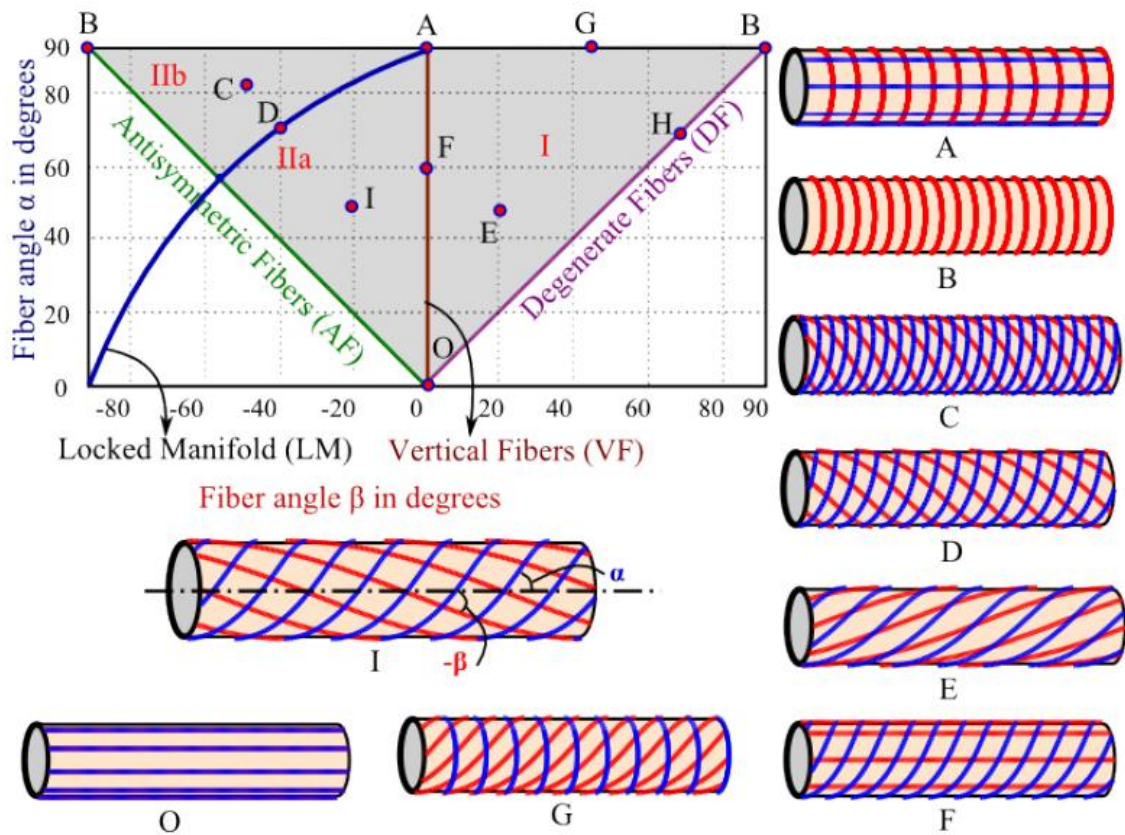
Figure 1-2. Design space spanned by the fiber angles in FREEs with example geometries in each quadrant (Reproduced from [5]).

1.3 Analysis of FREEs

Design and control of soft robots require analytical models that predict how soft structures deform. This thesis proposes a model to predict the static deformation behavior of FREEs. FREEs deform due to a complex interaction of pressurized fluids on stretchable cylindrical enclosures reinforced by interlacing patterns of fibers. Existing models that capture FREE deformations and exerted forces or torques involve simplifications, or may be valid for a specialized reinforced fiber

orientation. This thesis proposes a generalized formulation that can capture deformation behavior of FREEs with arbitrary and varying fiber orientations. Furthermore, this formulation can seamlessly switch between quick analysis, which furthers design insight and high fidelity analysis that takes into account real constraints.

There are several models that predict deformation of PAMs with varying level of accuracy. Most simple models assume the undeformed and deformed configuration to be pure cylinders leading to closed form equations for deformation and actuation forces. Kothera et al. [7] use cylindrical assumptions and compare two formulations: (a) energy based model, and (b) force balance based model, and conclude that the latter model matches better with experimental results. Liu and Rahn [4] analyze the axisymmetric deformation of conventional PAMs using large deformation membrane theory and predict actual curvilinear deformation and forces. Shan et al. [3] analyze the deformation of PAMs made of a fiber reinforced matrix composite membrane. Both these models use equilibrium equations based on force balance, and though accurate are valid for PAMs where the fiber orientations are equal and opposite.

FREEs however permit arbitrary variation of fiber orientations (see Figure 1-1b) of which the PAM configuration is only a special case. This not only broadens the design space, but also enables unique motion patterns such as axial rotation and screw motion that are otherwise unattainable with conventional actuators (see Figure 1-1d). These actuators also find use in endoscopes, pipe inspections and wearable robots [8]. Existing models that expose the prowess of FREEs are limited to pure cylindrical assumptions leading to greater than 20% inaccuracy in predicting actuation forces/ torques and deformation. Connolly et al. [8] use finite element analysis to predict the deformation behavior of FREEs with asymmetric fiber angles, and present parametric insights for potential use in design. Though useful, these models may be

5

computationally intensive, requiring commercial FEA solvers. They yield little insight on the inherent mechanics of deformation.

1.4   Scope of the Thesis

Main goal of this thesis is to develop an analysis framework to analyze the deformation behavior of FREEs. Towards this, a generalized energy-based model to predict the deformation of FREEs with any arbitrary fiber orientations is developed. This model is built on observing the deformation of inflatable objects such as balloons [9], soap bubbles, and water droplets, which evolve due to an inherent drive to enclose maximum volume limited by physical constraints posed by material or an external agency. Such a constrained volume maximization for FREEs is posed in this thesis as a calculus of variations problem, which is readily solvable using known numerical tools [10]. The advantage of this formulation lies in its ability to maximally decouple kinematics and kinetostatics. Kinematics deals with the determination of the deformed shape independent of the material properties and manufacturing, leading to a computationally less intense problem. Kinetostatics relates deformation to the actuation pressure and external load, and requires estimation of material properties, and overall size. Based on the fidelity of the analysis required, realistic considerations such as fiber extensibility can also be considered in kinetostatics. Furthermore, the advantage of the formulation is in the ability to treat arbitrary fiber angles apart from those that span the configurations of the popular pneumatic artificial muscle. This analysis framework can be generalized to analyze any inflatable body or device with physical constraints limiting its volume expansion.

6

FREEs being soft pneumatic actuators are compliant, flexible, and can conform to or wrap around arbitrary contours. They also pose minimal injury threats to users in case of failure. This makes them an appropriate choice for use as a source of actuation in human assistive devices. Towards this, a design of an upper arm orthosis utilizing a FREE is demonstrated in Chapter 3. Motivation of the design is to reduce wrist loading in crutch users to prevent wrist injuries. FREEs can provide the actuation for this task while being light enough to be wearable by the user without any hindrance to everyday activities. A design methodology that utilizes the analysis framework developed in this thesis is shown. This methodology can be used to design devices that use FREEs for actuation particularly for human assistive devices.

1.5   Organization of the Thesis

The thesis introduces an analysis framework for analyzing FREEs with any fiber configuration and geometry. Chapter 2 presents all the details of the analysis methodology starting with stating the constrained volume maximization problem that needs to be solved for analysis. Different constraints imposed on the problem and their physical interpretation is shown. Furthermore, solutions of the model along with analogy with virtual work method is shown. Deformation of McKibben FREEs or PAMs under applied pressure and external forces is analyzed using the model and thereafter is validated with existing models for accuracy and with experiments on a custom-fabricated actuator. This is followed by analysis and experimental validation of the deformation of rotating-contracting FREEs under applied pressure and external torques. It is further shown that novel FREEs such as purely rotating actuator whose fiber angles vary arbitrarily along its length can also be analyzed using this framework.

Chapter 3 presents the design of an upper arm sleeve orthosis. The orthosis is designed to reduce wrist loading of crutch users to prevent wrist injuries. Details of the design are presented along with the advantages of using FREE as the source of actuation. The analysis framework developed in Chapter 2 along with a string model introduced in Chapter 3 is used to analyze the performance of the sleeve. Conclusions, summary of the contributions, and future directions or extensions of the work are detailed in Chapter 4.

2. Analysis of Fiber Reinforced Elastomeric Enclosures

2.1   Constrained Maximization Formulation

Any inflatable device such as a balloon or a bellow assumes a deformed shape that tends to maximize its enclosed volume. However, indefinite increase in volume is limited by a physical constraint [11]. For example, a soap bubble assumes a spherical shape as it encloses maximum volume for a given surface area constraint. This configuration minimizes its free energy and ensures stability. Several examples in nature such as the shape of biological cells are testimonial of such a constrained maximization.

In this chapter, it is proposed that the FREE deformation is also governed by constrained volume maximization. In FREEs with two families of helical fibers (see Figure 2-1), the constraint is geometric in nature, enforced by the inextensibility of fibers along their arc length [5]. Such a length constraint has been previously used in predicting the deformed shape of a mylar balloon [9]. In this section, a generalized model to obtain the deformed shape of FREEs by posing a calculus of variations problem is formulated: *determine the deformation parameters of a FREE that maximize its enclosed volume while conserving its fiber length, under an external load (force/torque) and a given strain energy stored in the elastomer*.

The author would like to emphasize that such a formulation has the following distinct advantages: **(i)** No assumptions required on the deformed and undeformed configurations (such as a uniform cylinder geometry), **(ii)** no assumptions on the fiber angles (can be arbitrary, varying uniformly, varying discretely etc.) except the degenerate case resulting in a single family of fibers $\alpha = \beta$, and **(iii)** accurately captures boundary conditions due to end connectors.

2.1.1 Formulation
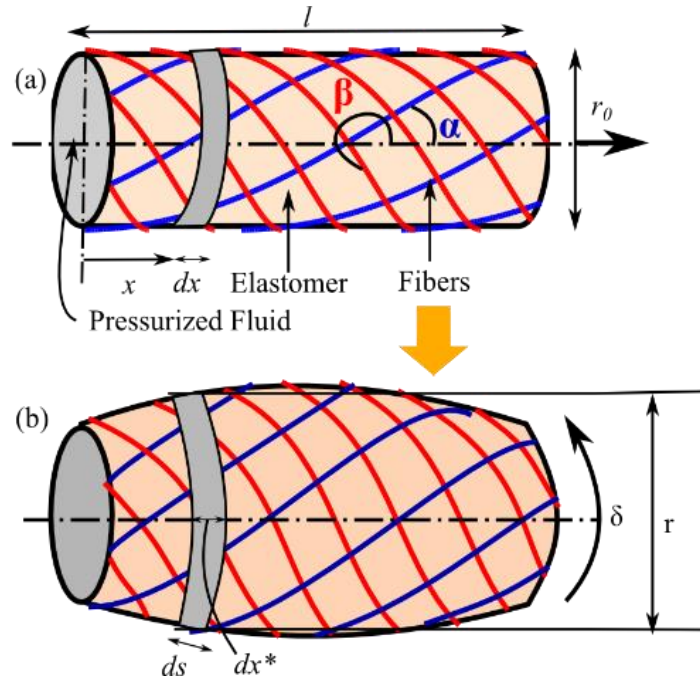
Figure 2-1 Undeformed (top) and deformed (bottom) configurations of FREE.

A FREE actuator is made of a hyper-elastic and incompressible cylindrical membrane, which is reinforced by two families of inextensible fibers as shown in Figure 2-1a. The two families of fibers are helically wrapped around the external surface of the cylindrical tube at angles α and β, where $\alpha \neq \beta$. Upon pressurization with fluids, the FREE deforms thereby extending or contracting in length accompanied by axial rotation and change in radius as shown in Figure 2-1b [5]. Conventional PAMs constitute a special class of FREEs that have their fibers wrapped with the relationship $\alpha = -\beta$. Because of this relationship, they contract or extend alone, without any rotation about its axis.

As shown in Figure 2-1, we consider a cylindrical actuator having an undeformed radius, r_0 and length, l. Deformation of the actuator is characterized by the axial and circumferential

stretch ratios, λ_1 and λ_2, respectively, which are Eigenvalues of the Green strain tensor. To capture generality, they are considered to be functions of membrane coordinates along the axial direction, x and are given by

$$\lambda_1(x) = \frac{ds}{dx} \text{ and } \lambda_2(x) = \frac{r(x)}{r_0} \tag{2.1}$$

In Equation 2.1, ds is elemental length along the deformed meridian direction, while dx is the elemental length along the undeformed axial direction, which is the same as the undeformed meridian direction. The third stretch ratio $\lambda_3(x) = 1/(\lambda_2(x)\lambda_1(x))$ is along the thickness of the elastomer and ensures incompressibility of the elastomer. Finally, a fourth parameter is $\delta(x)$, which is the elemental axial rotation of the FREE at some distance x from the fixed end. The general all-encompassing constrained maximization formulation for a FREE can be stated as

$$\underset{\lambda_1(x), \lambda_2(x), \delta(x)}{\text{Max}} \quad V = \int_0^l \pi r_0^2 \lambda_2^2(x) \sqrt{\lambda_1^2(x) - \lambda_2'^2(x) r_0^2} \, dx \tag{2.2}$$

Subject to

$$\lambda_1^2(x)\cos^2 \alpha(x) + \lambda_2^2(x)\sin^2 \alpha(x) \left(\frac{\theta + \delta(x)}{\theta} \right)^2 = \gamma^2 \tag{2.3}$$

$$\lambda_1^2(x)\cos^2 \beta(x) + \lambda_2^2(x)\sin^2 \beta(x) \left(\frac{\phi + \delta(x)}{\phi} \right)^2 = \gamma^2 \tag{2.4}$$

$$W = \int_0^l A_e (C_{10}(I_1 - 3) + C_{01}(I_2 - 3)) dx, \text{ where } 0 \le W \le W_l \tag{2.5}$$

$$l_d = \int_0^l \sqrt{\lambda_1^2(x) - \lambda_2'^2(x) r_0^2} \, dx, \text{ where } l_l \le l_d \le l \tag{2.6}$$

$$\delta_d = \int_0^l \delta(x) dx , \text{ where } 0 \le \delta_d \le \delta_l \tag{2.7}$$

where, the volume is expressed in terms of the curvilinear deformed profile of the actuator and is consistent with Shan et al. [3]. Equations 2.3 and 2.4 denote the constraints imposed from conserving the length of the fiber albeit with some extensibility as derived in Krishnan et al. [5]. Here the fiber angles $\alpha(x)$ and $\beta(x)$ are considered with explicit dependence on x. The terms θ and ϕ indicate the number of turns made by the fibers on the circumference of the cylinder. The term γ denotes the extensibility of fibers, which is the fraction of increase in its overall length. This term would be one if the fibers are inextensible. In Equation 2.5, W denotes the strain energy stored in the elastomer assuming a Mooney-Rivlin hyperelastic model, where the strain energy density depends on constants C_{10} and C_{01} associated with the first two strain invariants $I_1 = \lambda_1^2 + \lambda_2^2 + \lambda_3^2$ and $I_2 = \lambda_1^2 \lambda_2^2 + \lambda_1^2 \lambda_3^2 + \lambda_2^2 \lambda_3^2$. Here, A_e denotes the cross section area of the elastomer material in the undeformed configuration. The maximum value that W can attain is in its maximum deformable configuration or the locked configuration and is denoted by W_l. In Equation 2.6, l_d is the stroke of the actuator, which is the change in its axial length. For contracting FREEs, the stroke must be greater than its maximum attainable value in the locked configuration denoted by l_l. Similarly, δ_d is the net axial rotation at the free end of the actuator, and is bounded by a maximum value at the locked configuration δ_l.

2.1.2 Solution through Virtual Work Analogy

The constrained maximization formulation of Equations 2.2-2.7 is a calculus of variations problem subject to three variables $\lambda_1(x)$, $\lambda_2(x)$, and $\delta(x)$. Out of these we can readily eliminate $\lambda_1(x)$ and $\delta(x)$ by expressing it in terms of $\lambda_2(x)$ by solving Equations 2.3 and 2.4 simultaneously. We thus seek to find an optimal $\lambda_2(x)$ that maximizes Equation 2.2 subject to constraints posed by Equations 2.3-2.7. For such a problem, the generalized Euler-Lagrange equations can be given by

$$\Delta V + \Lambda_1 \Delta W + \Lambda_2 \Delta l_d + \Lambda_3 \Delta \delta_d = 0 \tag{2.8}$$

where Δ is an operator denoting the first variation of a functional according to the rules of calculus of variation.

$$\Delta = \frac{\partial}{\partial \lambda_2(x)} - \frac{\partial}{\partial x}\left(\frac{\partial}{\partial \lambda_2'(x)}\right) \tag{2.9}$$

and Λ_i; $i = 1..3$ are the Lagrange multipliers associated with the constraints and can be rewritten as

$$\Lambda_1 = -\frac{1}{P}, \ \Lambda_2 = -\frac{F}{P}, \ \Lambda_3 = -\frac{M}{P} \tag{2.10}$$

Substituting Equation 2.10 in Equation 2.8 yields

$$P\Delta V = \Delta W + F\Delta l_d + M\Delta \delta_d \tag{2.11}$$

where, now using the virtual work analogy, P can be interpreted as the applied pressure, F is the applied end load, and M is the applied end moment. Solution of Equation 2.11 can yield the

deformed profile for a given P, F, and M. Thus, the constrained maximization approach is analogous to the energy-based method and circumvents the need for classical force-equilibrium based governing equations. In the next section, we shall deal with purely the kinematic parts of the formulation to predict the maximum achievable deformation of a FREE.

2.2   Kinematics: Locked Configuration

Every FREE actuator with two families of reinforced fibers deforms upon application of internal pressure. This deformation was shown by [5] to be bounded by a maximum deformed shape, which is known as the locked configuration. The locked configuration can be obtained from the constrained maximization formulation by solving Equation 2.2 subject to constraints of Equations 2.3 and 2.4. As explained in the previous section, the above problem can be converted to an unconstrained optimization form by expressing $\lambda_1(x)$ and $\delta(x)$ in terms of $\lambda_2(x)$ by solving Equations 2.3 and 2.4. For an unconstrained maximization problem, there is only one necessary condition which is given by [12].

$$\frac{\partial V}{\partial \lambda_2(x)} - \frac{\partial}{\partial x}\left(\frac{\partial V}{\partial \lambda_2'(x)}\right) = 0 \tag{2.12}$$

In addition, there are two boundary conditions for this problem, both of which constrain radial expansion at the ends of the actuator due to the end connectors. Fixed radius implies that λ_2 is unity at both the ends.

$$\lambda_2(0) = 1 \text{ and } \lambda_2(l) = 1 \tag{2.13}$$

14

The solver 'bvp4c' in MATLAB integrates a system of ordinary differential equation subjected to two-point boundary value conditions and is therefore appropriate to solve Equation 2.12 with boundary conditions given by Equation 2.13. Its solution yields an optimal radial stretch-ratio function $\lambda_2(x)$, which together with $\lambda_1(x)$ from Equations 2.3 and 2.4 can plot the deformed locked shape of the actuator. Figure 2-2 (shown in red) shows such a deformed shape for a conventional PAM actuator whose initial fiber angles (shown in in blue) were $\alpha = -\beta = 30°$. Figure 2-3 shows the locked shape of a FREE with initial fiber angles $\alpha = 0°$ and $\beta = 30°$ (shown in blue) that is plotted using the optimal $\lambda_1(x)$ and $\lambda_2(x)$. The axial rotation of the free end with respect to the fixed end is obtained by integrating $\delta(x)$ over the length of the actuator. Obtaining the locked configuration is usually quick and can facilitate design.
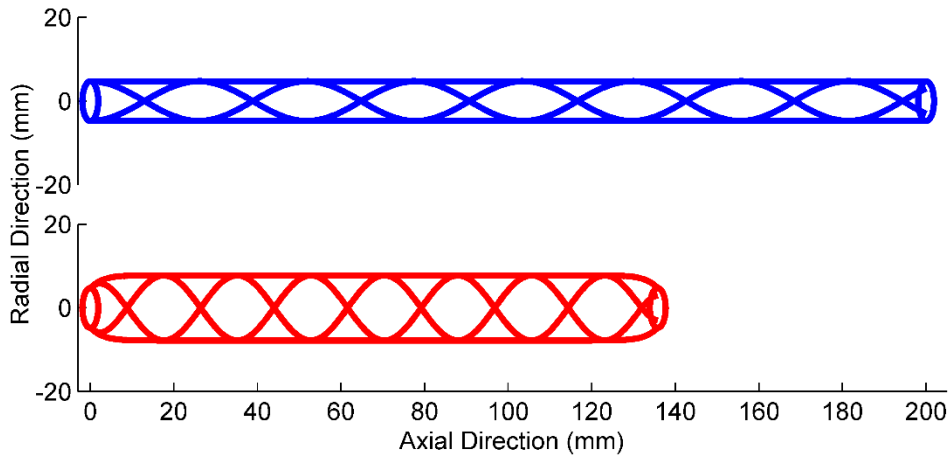
Figure 2-2. Undeformed (top, blue) and deformed (bottom, red) shape of conventional PAM actuator with $\alpha = 30°$.
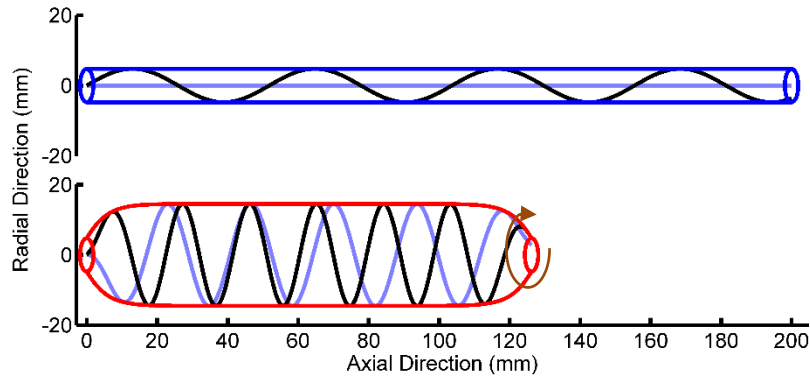
Figure 2-3. Undeformed (top, blue) and deformed (bottom, red) shape of contracting-rotating FREE actuator with $\alpha = 0°$ and $\beta = 30°$.

Apart from the change in actuator shape captured in Figure 2-2 and Figure 2-3, there is an accompanying change in the fiber orientations from their initial values. This change is pronounced in Figure 2-3 where an initially straight fiber (shown blue) turns helical upon deformation. The change in fiber orientations under purely cylindrical assumptions was explained in [5] within a FREE design space spanned by fiber angles α and β as shown in Figure 2-4. It was proved in [5] that the fiber orientation when locked lies in a one-dimensional manifold, known as the locked manifold (shown as the blue line in Figure 2-4). Here, we show the validity of this manifold even by relaxing the cylindrical assumption. Four FREEs with different initial fiber angles are marked in blue in Figure 2-4. The corresponding fiber orientations in the deformed configuration found by solving (6) are marked in red in Figure 2-4. The deformed fiber orientations lie on the locked manifold.
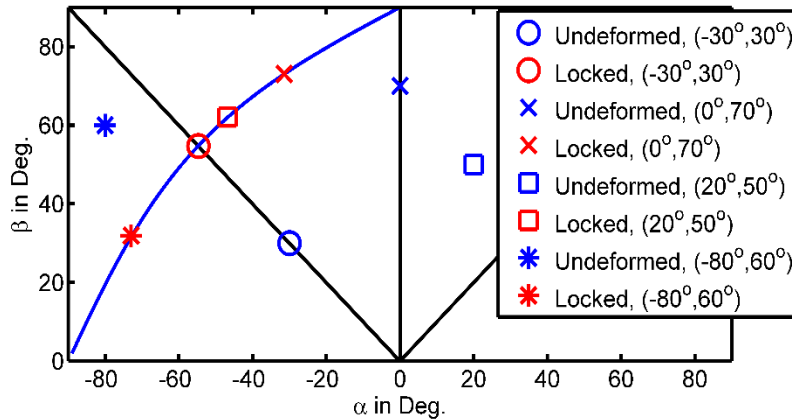
Figure 2-4. Locked fiber configurations obtained by the model for actuators with different fiber angles.

Though the locked manifold is unaffected by the curvilinear deformation shape, the same is not true for the deformation parameters. For example, a uniform cylindrical approximation approach from [5], [6] yields 15% more axial rotation in the locked configuration for the FREE presented in Figure 2-3. This substantiates the need for obtaining exact curvilinear deformed profiles.

2.3   Kinetostatics of McKibben FREEs

In this section, we analyze the kinetostatic behavior of McKibben FREEs and experimentally verify it by comparing with fabricated prototypes. We compare the prototype with our analytical model for three quantities: (a) actuation pressure vs. stroke length, (b) blocked force vs. actuation pressure, and (c) force vs. stroke length. Axial force required to prevent any contraction is called the blocked force. In other words, blocked force prevents any change in length

17

of actuator when the pressure is applied. These constitue the *kinetostatic* deformation behavior as they are dependent not just on the fiber kinematics but also the elastomer material properties and applied forces.

Mckibben actuators, as discussed in the introduction constitute a special class of FREEs that have the two families of fibers at angles α and β with $\alpha = -\beta$. Substituting this in Equations 2.3 and 2.4 yield a single fiber inextensibility equation with no axial rotation $\delta(x) = 0$ given by

$$\lambda_1^2 (x) \cos^2 \alpha + \lambda_2^2 (x) \sin^2 \alpha = 1^2 \tag{2.14}$$

The locked configuration of such an actuator is shown in Figure 2-2. However, for most practical applications, we are interested in the deformation of the McKibben actuator as a function of applied pressure, and under applied external forces.

2.3.1 Comparison with Fiber-Reinforced Composite Model

We first compare the solution from our formulation with a comprehensive flexible matrix composite model developed by Shan et al. [3] for nonlinear axisymmetric deformation of composite PAMs. Two PAMs with initial fiber angles $15°$ and $25°$ are considered. An anisotropic material model given by Eq. 16 - 54 in [3] was used.

Solving Equation 2.2 subjected to Equations 2.5 and 2.14 for various strain energy fractions yields several intermediate configurations. An intermediate configuration is selected for these actuators such that the deformed stroke length matches exactly with the demonstrated model in [3]. The corresponding Lagrange multiplier yields the value of applied pressure according to

Equation 2.11. Figure 2-5 compares the deformed profiles for half the length and diameter of both these actuators. The results match closely with the maximum error at certain regions under 5%. These small deviations may be due to transverse bending stiffness incorporated into the analysis of the matrix composites [3]. The corresponding pressure values at which the deflection is attained matches to less than 10% error. With the accuracy of the model ascertained, we now compare our model with experimental results obtained from custom-fabricated McKibben FREEs.
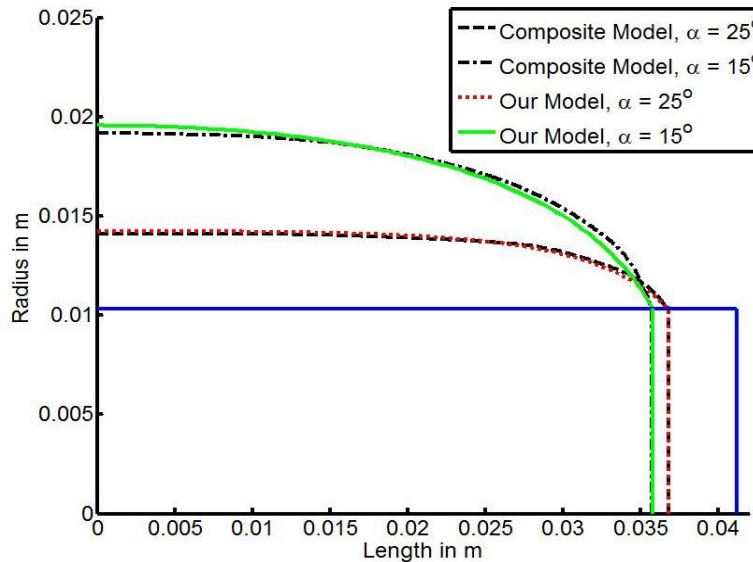
Figure 2-5. Comparison with Shan et al.'s [3] model for McKibben actuator for 0.1 MPa actuation pressure.

2.3.2 Actuator Fabrication and Experimental Setup

We fabricated three contracting McKibben FREEs, each having an inner radius of 4.76 mm and a wall thickness of 1.59 mm. Fiber angles of the three actuators are 30°, 35°, and 40°. Length

of actuators with fiber angles 30º and 35º is 192 mm each, while 40º actuator has a length of 193 mm. The FREE prototypes are created using a custom in-house fabrication process similar to [5], [6]. Their fabrication starts with a base layer of natural rubber latex tubing with 0.794 *mm* wall thickness (Kent Elastomer). Fibers are then wound in a semi-automated fashion with the desired angle and orientation. Adhesive agents are applied to cement fibers on the latex tube.

Two testbeds were fabricated to measure the three kinetostatic deformation parameters for the McKibben actuators as shown in Figure 2-6. The first setup shown in Figure 2-6a consists of a load cell and a pressure gauge, which is used to measure the axial force generated by FREE at different actuation pressures and stroke lengths. Second setup shown in Figure 2-6b consists of a linear encoder to measure the stroke, rotary encoder to measure rotation, and a pressure sensor to record the input pressure. Results of the experiments conducted are detailed below.
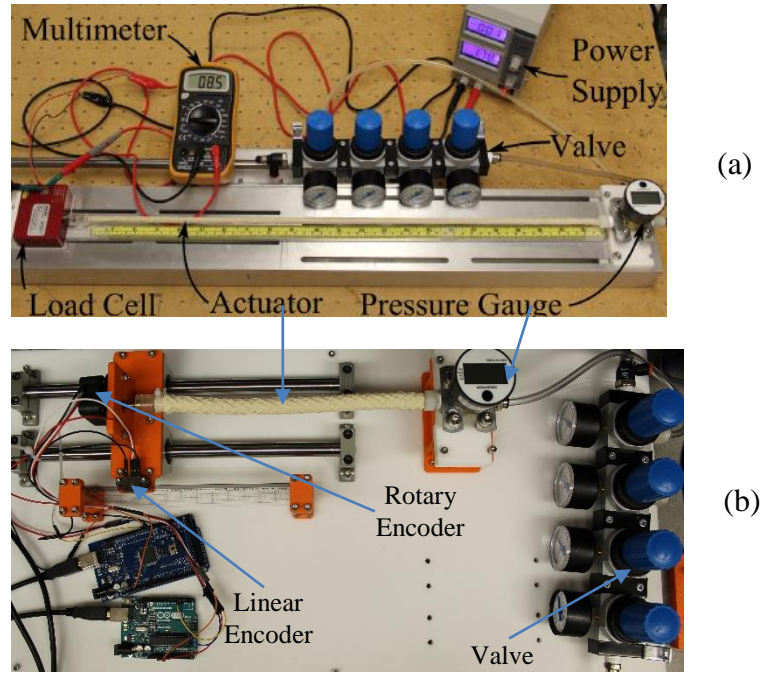
Figure 2-6. Experimental setup to measure the kinetostatic quantities of a McKibben FREE actuator

2.3.3 Actuator Pressure vs. Deformation

In this section, we determine the material constants of the elastomer by comparing the experimental deformed lengths or stroke as a function of pressure with the analytical values. Experimentally, we obtain this by varying the input pressure in the setup of Figure 2-6b and obtaining the reading from the linear encoder without restricting its end motion for the three McKibben FREEs. This input pressure vs actuator length is plotted in Figure 2-7 by different markers.
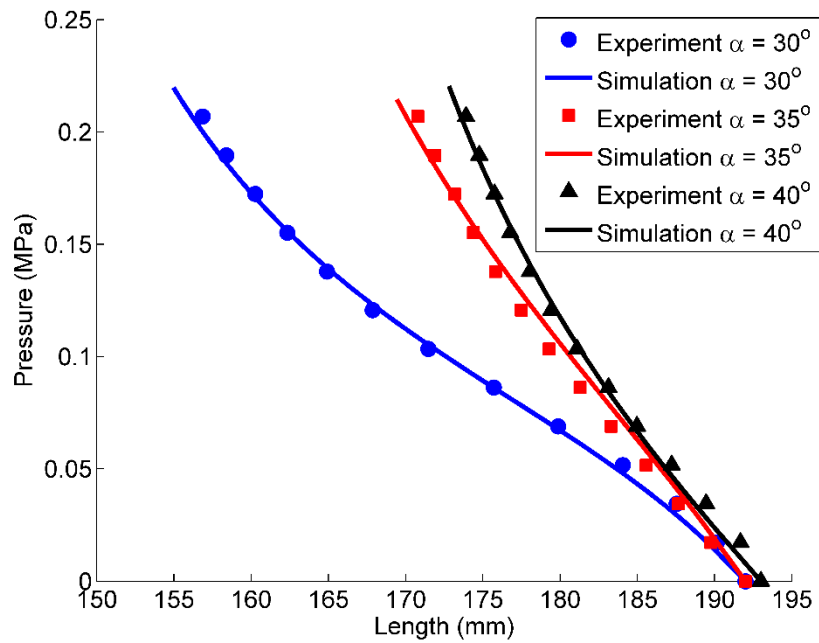
Figure 2-7. Actuation pressure vs. stroke length for a contracting McKibben actuators with different fiber angles.

Table 1. Elastic Constants obtained for the three McKibben FREEs

Fiber Angle	C_{10}	C_{01}
30°	0.11	0.06
35°	0.18	0.12
40°	0.18	0.1

To obtain the deformed configuration of the McKibben FREE analytically as a function of the applied pressure we solve Equation 2.2 subject to Equations 2.14 and 2.5. Equation 2.5 deals with the strain energy stored, and requires two elastic constants C_{10} and C_{01}, which are in general functions of the elastomer and experimentally determined. The solution boils down to a part of Equation 2.11 given by

$$P\Delta V = \Delta W \tag{2.15}$$

where P is the applied pressure and Δ is defined in Equation 2.9, and W is the strain energy stored as given in Equation 2.5. The above differential equation is solved in MATLAB using the boundary condition given by Equation 2.13. This leads to a function $\lambda_2(x)$, which when substituted in Equation 2.14 yields $\lambda_1(x)$ for a given actuation pressure P. The deformed axial length, or stroke of the actuator is given by Equation 2.6, and is plotted with respect to applied pressure as the thick lines in Figure 2-7. It must be noted that that values of the elastic constants C_{10} and C_{01} are adjusted to match the experimental values. Their values as shown in Table 1 are the same for 35^0 and 40^0 case, but differs considerably for the 30^0 due to variations in manufacturing. However, the validity of the formulation is established as the nature of the analytical curve matches with that of experiments. Furthermore the deformed shape of the McKibben FREE for various pressures matches very closely with both experiments [13] and the force-equilibrium based formulation using fiber-reinforced models [3].

2.3.4 Blocked Force vs. Applied Pressure

The operational benefits of using McKibben FREEs in robotics deals with its ability to provide actuation forces. Here, we measure the actuation forces as blocked forces or the external force applied to the actuator to take it to the undeformed configuration. This is equivalent to experimentally fixing the length of the actuator and measuring the reaction force at the load cell as shown in Figure 2-6a. The experimental results for the blocked force as a function of pressure for the three McKibben FREEs are shown by different markers in Figure 2-8.
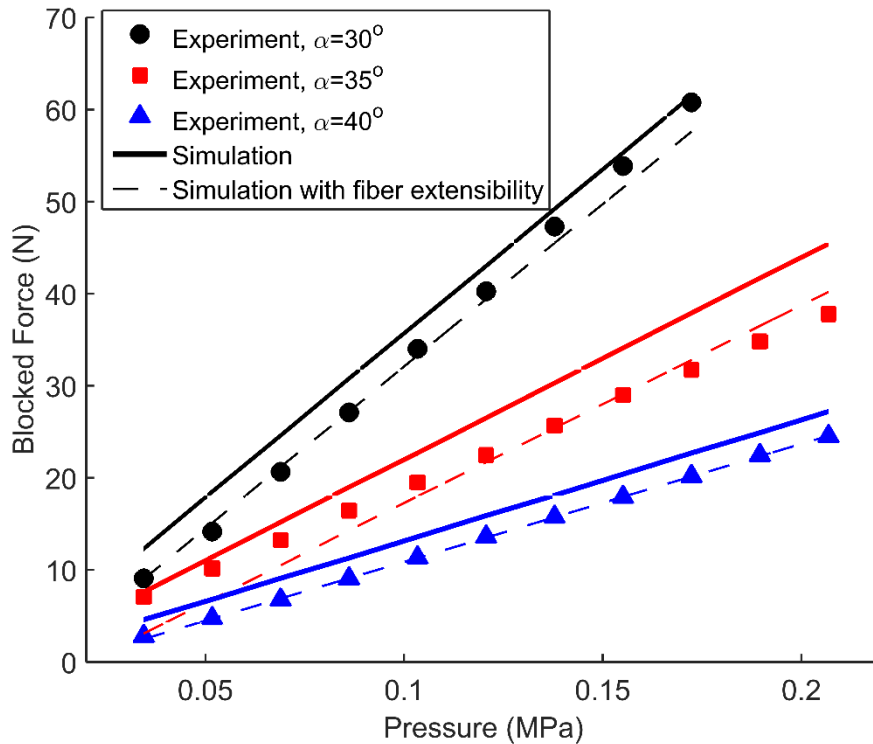
Figure 2-8. Blocked force vs actuation pressure for three different McKibben actuators.

For analytically determining the blocked force, we solve Equation 2.2 subject to Equations 2.14, 2.5, and 2.6 such that l_d in Equation 2.6 is equal to the undeformed length l. The

24

corresponding Lagrange multiplier gives the blocked force. The blocked force can be obtained by solving the following part of Equation 2.11 at the instant deformation begins, and is given by

$$P\int_0^l \Delta V \bigg|_{\lambda_2 \to 1} dx = A_e \int_0^l \Delta W \bigg|_{\lambda_2 \to 1} dx + F\int_0^l \Delta l_d \bigg|_{\lambda_2 \to 1} dx \qquad (2.16)$$

here $\lambda_2(x) \to 1$ denotes instantaneous deformation. At this instant, usually $\Delta W \to 0$, which makes the analytical blocked force independent of the material properties. This blocked force is plotted as thick lines in Figure 2-8.

Comparison of the analytical and experimental blocked force reveals a mismatch. This mismatch is consistent with the findings of Kothera et al. [7] on implementing the energy formulation. They later perform force-equilibrium based estimations and obtain better corelation with experiments. In this chapter, we show that the proposed energy-based formulation may also yield a good corelation, provided real operating conditions such as the extensibility of fibers are considered. The extensibility usually results because the fibers are not completely taut while and after winding. Thus some amount of actuation pressure is required to deform the cylinder such that the fibers are taut and indeed behave as inextensible elements. It must be noted that this is different from modeling the inherent stiffness of the fibers, which are at least two orders of magnitude greater than the elastomer. We modify the inextensibility constraint to take the form given by

$$\lambda_1^2(x)\cos^2\alpha + \lambda_2^2(x)\sin^2\alpha = \gamma^2 \qquad (2.17)$$

where γ represents the amount of extension undergone by the fibers. In case of perfect inextensibility, γ equals one and in case of entension it is larger than one with rest of the analysis staying the same. We introduce an extension of 0.5% for the 30º actuator and 0.75% for both 35º

25

and 40º actuators. Including fiber extension in our model reduces the offset error to almost zero. Blocked force obtained for the three actuators with fiber extensibility is shown in Figure 2-8 using dotted lines.

2.3.5 Force vs. Actuator Length (Stroke)

Here we determine the length of the deformed McKibben FREE for a given applied pressure and given external force. These values are experimentally obtained by first locking the length at different values between its undeformed length and the maximum deformed length. The reaction force from the load cell in Figure 2-6a is obtained at different pressures. The reaction force is plotted as a function of the actuator length for different pressures in Figure 2-9 for different McKibben actuators.

Analytical estimate of the force vs. actuator length is obtained by solving Equation 2.2 subject to Equation 2.17 that includes fiber extensibility and Equations 2.5 and 2.6. Solving this gives the following differential equation with respect to $\lambda_2(x)$

$$P\Delta V = \Delta W + F\Delta l_d \tag{2.18}$$

subject to the boundary condition of Equation 2.13. Here, pressure P and force F are the known variables and solving Equation 2.18 gives the deformed length l_d as a function of the applied force F. These are plotted, first assuming the inextensibility of fibers with $\gamma = 1$ as solid thick lines in Figure 2-9. Assuming the same amount of extensibility as for Figure 2-8 yields a new set of values plotted as dotted lines in Figure 2-9. The assumption of extensibility yields better match with the

26

experimental results, especially at higher pressures. The obtained results are closer to the experimental values than the findings of Kothera et al. [7] for their energy-based formulations. These curves provide the performance graphs of the actuator, and can guide the designer in picking an actuator for a given application.
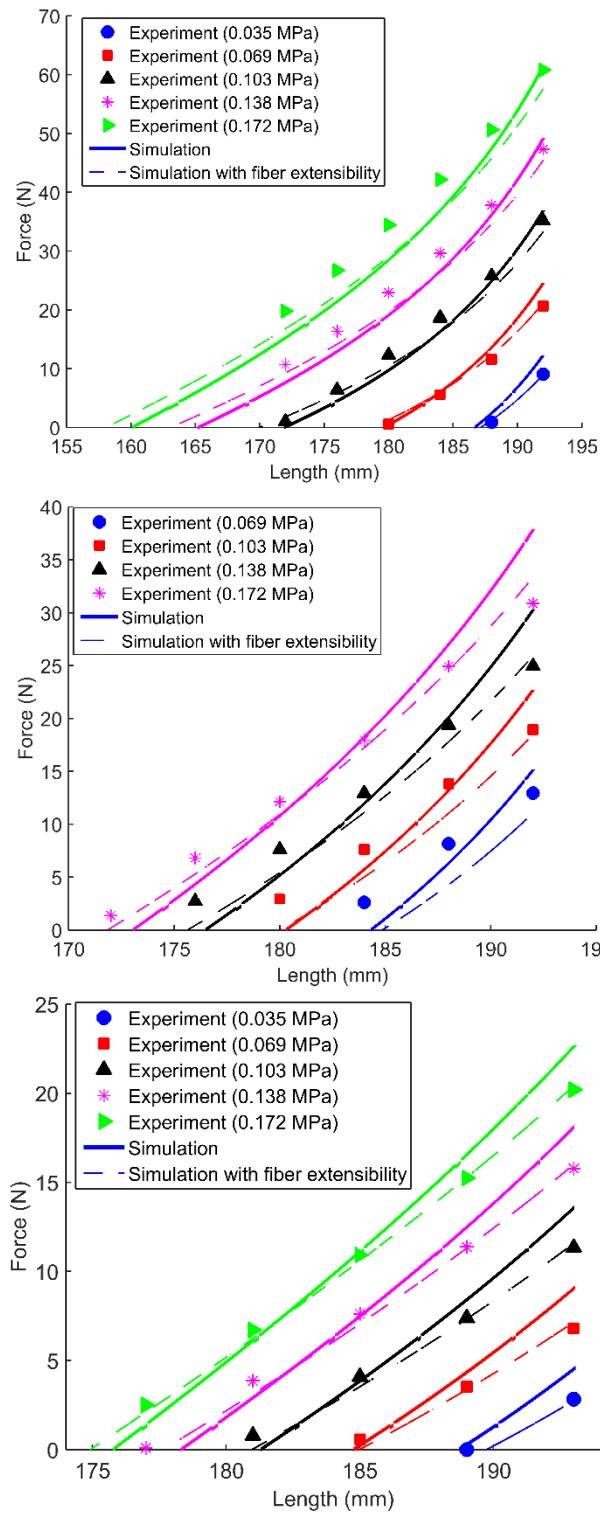
Figure 2-9. Force vs. Actuator Length for different actuation pressures (a) 30$^{\text{o}}$ actuator, (b) 35$^{\text{o}}$ actuator, and (c) 40$^{\text{o}}$ actuator.

2.4   Kinetostatics of Rotating FREEs

Similar to the previous section, here we show the analysis and experimental verification of rotating FREE actuators. We fabricated three rotating FREE actuators for experimental verification. All three prototypes have an inner radius of 4.76 mm and a wall thickness of 1.59 mm. Fiber angles and length of these three prototypes are:

Prototype A: $\alpha = 10°$, $\beta = 50°$, and $l = 141\ mm$.

Prototype B: $\alpha = 0°$, $\beta = 30°$, and $l = 131\ mm$.

Prototype C: $\alpha = 0°$, $\beta = 60°$, and $l = 143\ mm$.

2.4.1 Actuation Pressure vs. Deformation

In this section, we determine the stroke length and rotation of FREEs as a function of applied pressure. Prototypes B and C are contracting-rotating FREEs. They have a screw type motion, where rotation is coupled with contraction. Prototype A has a complex motion pattern, where it initially extends and rotates, and then starts contracting beyond a certain pressure. We obtain the stroke length and rotation from the linear and rotary encoders, respectively shown in Figure 2-6b. Figure 2-10a shows the variation of actuator length with pressure for the three prototypes. We can see that prototypes B and C contract with increase in pressure, whereas prototype A undergoes a small extension initially and starts contracting after a certain pressure.

To obtain the deformation behavior of rotating FREEs as a function of actuation pressure, we solve Equation 2.2 subjected to Equations 2.3-2.5. Solution method and boundary conditions are same as for McKibben FREEs. Solution yields $\lambda_2(x)$, which when substituted in Equations

2.3 and 2.4 give $\lambda_1(x)$ and $\delta(x)$. Stroke length and rotation are obtained by integrating Equation 2.6 and 2.7, respectively. As shown in Figure 2-10a, analytical result is able to capture the deformed actuator length for all three prototypes including prototype A, which initially extends and then contracts. Furthermore, the axial contraction is less than 5% of the length up to 0.1 *MPa* pressure for prototype B and up to 0.2 *MPa* for prototype C. Figure 2-11 shows a comparison between analytical and experimental deformation profiles for three actuation pressures to capture the initial extension and eventual contraction of FREE prototype A.

Figure 2-10b plots the axial rotation as a function of pressure for the three prototypes. The analysis results match well for all three cases for up to two full rotations and then deviates with a maximum error of 15%. The deviation can be explained due to the changes in elastomer properties at higher pressures, and inaccuracies in manufacturing.

2.4.2 Blocked Torque vs. Applied Pressure

The FREEs presented in this section primarily rotate about their axis similar to a motor. Thus, it is of interest to estimate the maximum torque generated as a function of pressure. In this case we shall focus on FREE prototypes B and C as they do not involve complex axial motion.
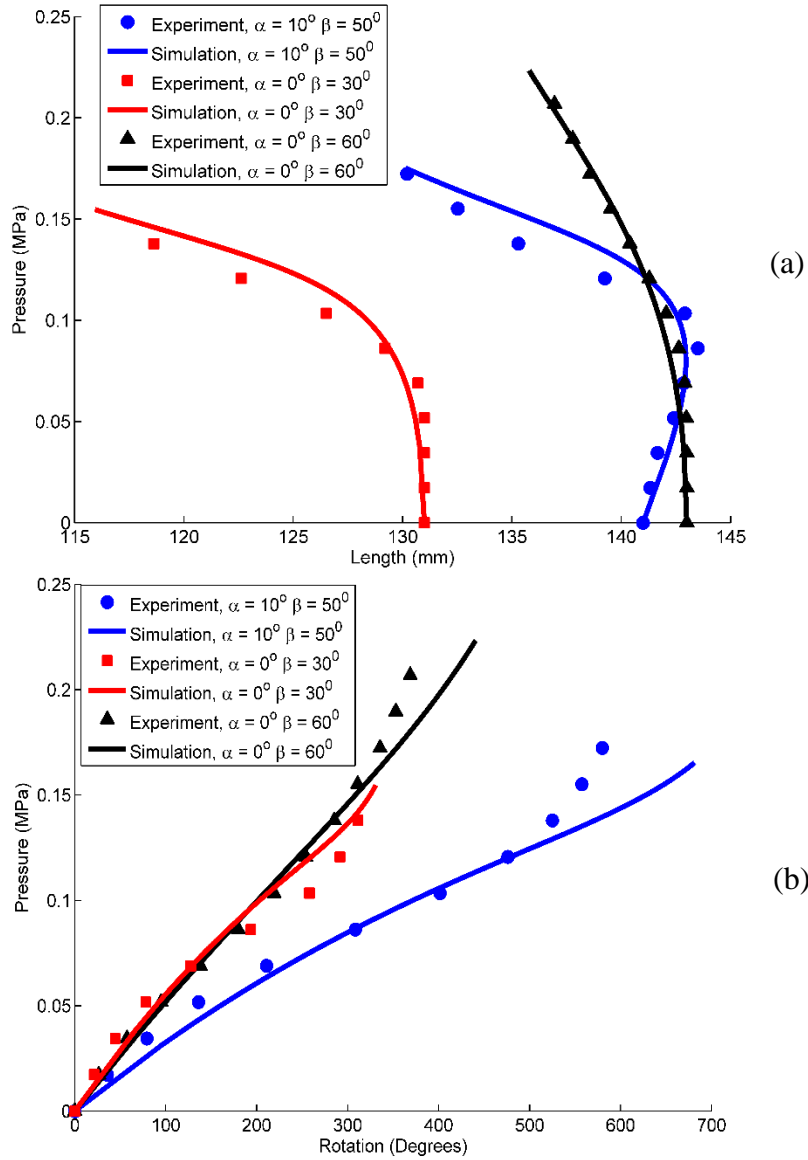
Figure 2-10. (a) Actuation pressure vs. stroke length and (b) actuation pressure vs. rotation for rotating FREE actuators with different fiber angles.

The blocked torque is measured by constraining both ends of the FREE actuator from rotating. A torque sensor is fixed at one end of the actuator, and is housed in railings to allow axial extension or elongation. Analytical estimate of the blocked torque is obtained from the constrained

31

maximization formulation by solving Equations 2.2, 2.3, 2.4, and 2.7 at the instant deformation

begins. This yields an equation similar to (16) given by

$$P \int_0^l \Delta V \mid_{\lambda_2 \to 1} dx = M \int_0^l \Delta \delta_d \mid_{\lambda_2 \to 1} dx \qquad (2.19)$$

In the above equation, the strain energy terms do not figure since no material energy is assumed

to be stored at this instant. Solving Equation 2.19 yields an algebraic expression for blocked torque

given by

$$M = \frac{2\pi r^3 P}{\tan \beta} \qquad (2.20)$$

where r is the inner radius of the actuator, β is one of the fiber angles with the other angle α

being 0^0, P is the applied pressure.

Figure 2-11. Analytical and experimental deformation of FREE prototype A at (a) 0 MPa
(undeformed), (b) 0.927 MPa, and (c) 0.138 MPa actuation pressure.

32

FREE Prototype B: The experimental blocked torque as a function of applied pressure is plotted in Figure 2-12a. It is seen that the initial torque is low, but it increases rapidly beyond $0.1\, MPa$. Furthermore, the experimental torque exceeds the analytical torque evaluated from Equation 2.20 at higher pressures. This may be counterintuitive, especially considering that Equation 2.20 is evaluated under ideal con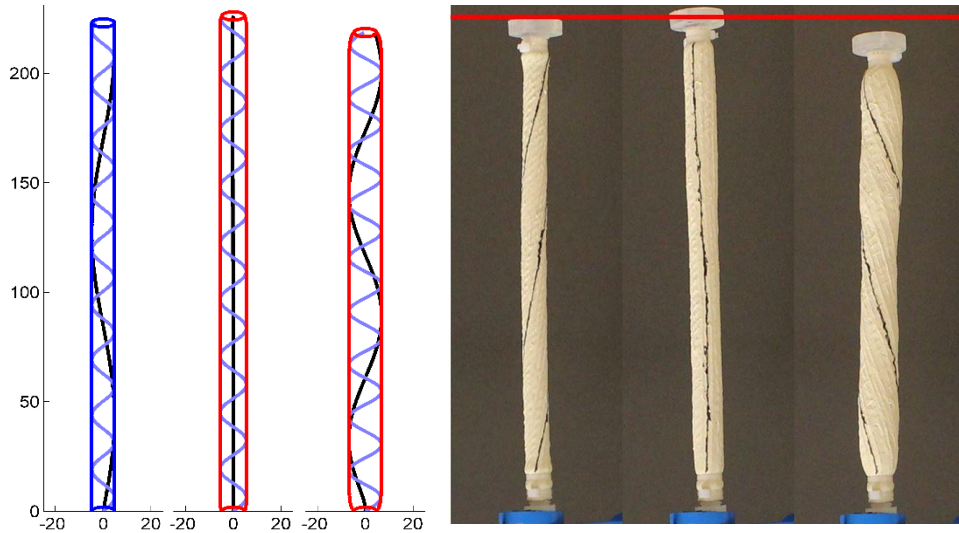ditions without fiber extensibility. We explain this increase in the blocked torque by a phenomenon called *blocked deformation,* which permits deformation of the FREE despite constraining its ends from rotation. Figure 2-13 shows this phenomenon for FREE Prototype B, where there is noticeable contraction of the FREE despite constraining end rotation.

The contraction of prototype B can be explained due to the FREE behaving as a McKibben contracting actuator with its end rotations constrained. Furthermore, the 0^0 fiber permits contraction as long as its length remains constant. Such a contraction may not occur in the ideal case where both fibers are tightly coupled. We propose to deal with this blocked deformation effect by superposing two stretch ratio fields: $\lambda_{2c}(x)$ due to contraction as seen in Figure 2-13 and $\lambda_{2r}(x)$ due to the instantaneous rotation yielding a torque.

$$\lambda_2(x) = \lambda_{2c}(x) + \lambda_{2r}(x) - 1 \tag{2.21}$$

where $\lambda_2(x)$ is the overall radial stretch ratio, which when substituted in Equation 2.2-2.7 yields terms due to both contraction and rotation effects. Out of these, $\lambda_{2c}(x)$ can be found experimentally from Figure 2-13, or by solving the McKibben problem of Equation 2.15. The blocked torque can then be found as

$$p\int_0^l \Delta_r V(x)|_{\lambda_{2r}(x)\to 1}\, dx = M_{corr}\int_0^l \Delta_r \delta_d(x)|_{\lambda_{2r}(x)\to 1}\, dx \qquad (2.22)$$

where Δ_r is the first variation given by (9), but with respect to $\lambda_{2r}(x)$, and M_{corr} is the corrected Torque. From Figure 2-12a, it is seen that the corrected torque is able to better match the experimental results. It must be noted that some fiber extensibility is assumed here to account for nearly zero measured torque at 0.03 MPa. In general, the experimental torque vs applied pressure has a larger slope than in Equation 2.20 because of increased initial expansion of its radius. Such an effect is also seen in the FREE prototype C with 0^0 and 60^0 fiber angles, where the experimental values are slightly larger than the analytical torque measured from Equation 2.20.

(a)

(b)
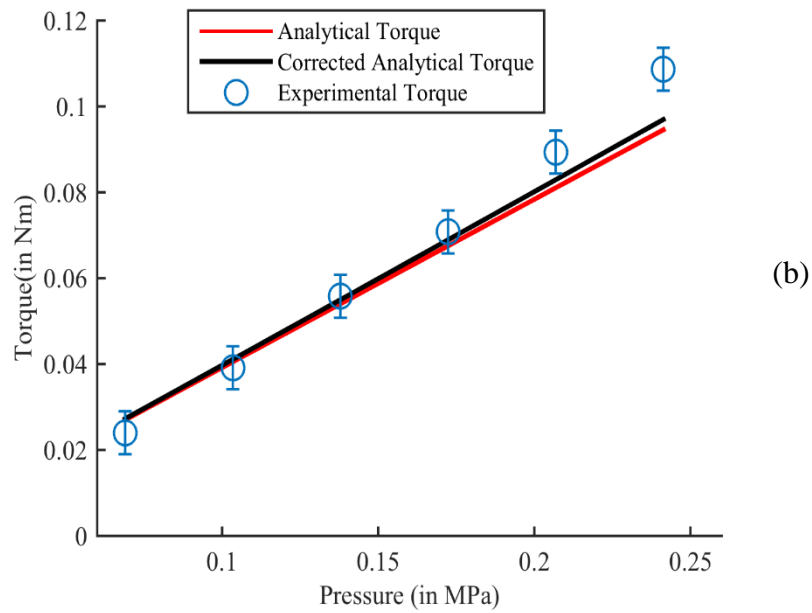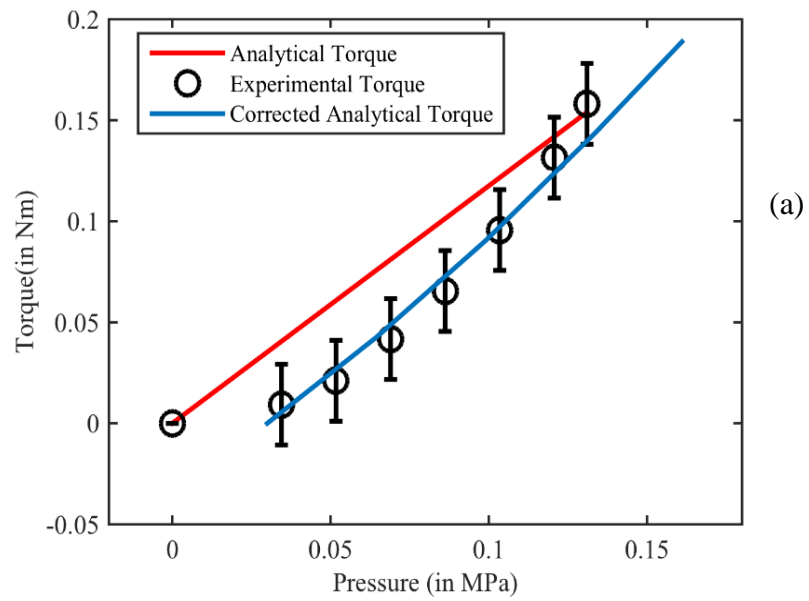
Figure 2-12. Torque vs. actuation pressure for rotating FREE with fiber angles (a) 0° and 30° and (b) 0° and 60°.
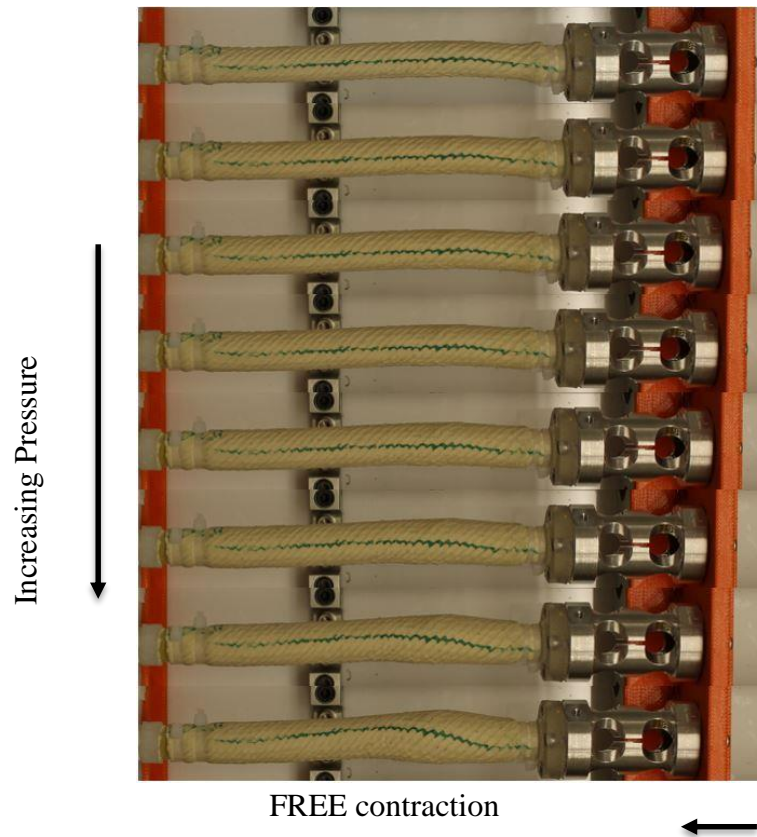
Figure 2-13. Blocked Deformation: Contraction of FREE prototype B with its end rotations constrained.

2.5   FREEs with Variable Geometries

The analysis methodology proposed in this paper is comprehensive, and valid for FREEs with any general fiber orientation. Furthermore, it relaxes several assumptions used to simplify the analysis in prior literature [5], [6], predominantly the uniform cylinder assumption. The generality of this analysis methodology proposed can enable conceptualization of novel fiber reinforced pneumatic actuators with arbitrarily varying anisotropy in its material properties.

2.5.1 FREEs with Varying Fiber Angles

In this section, we demonstrate an example of FREEs with fiber orientations varying along its length. In such cases, the fiber orientations α and β are not constants, but instead functions of coordinates along axial direction, such as the one shown in Figure 2-14.

For a conventional FREE actuator with asymmetric fiber angles, rotation is always coupled with extension or contraction as seen in the various intermediate deformed profiles of Figure 2-11. This implies that there cannot be a purely rotating FREE with constant fiber angles. But by varying the fiber angles, we can design a FREE that yields pure axial rotation. In Figure 2-14, we show an actuator whose fiber angles vary such that half of the actuator rotates and contracts and the other half extends. A preliminary demonstration of this was also presented in [13]. The variation of fiber angles is chosen so that the contraction in the rotating part cancels the extension, thereby conserving its overall length shown in Figure 2-14(a).
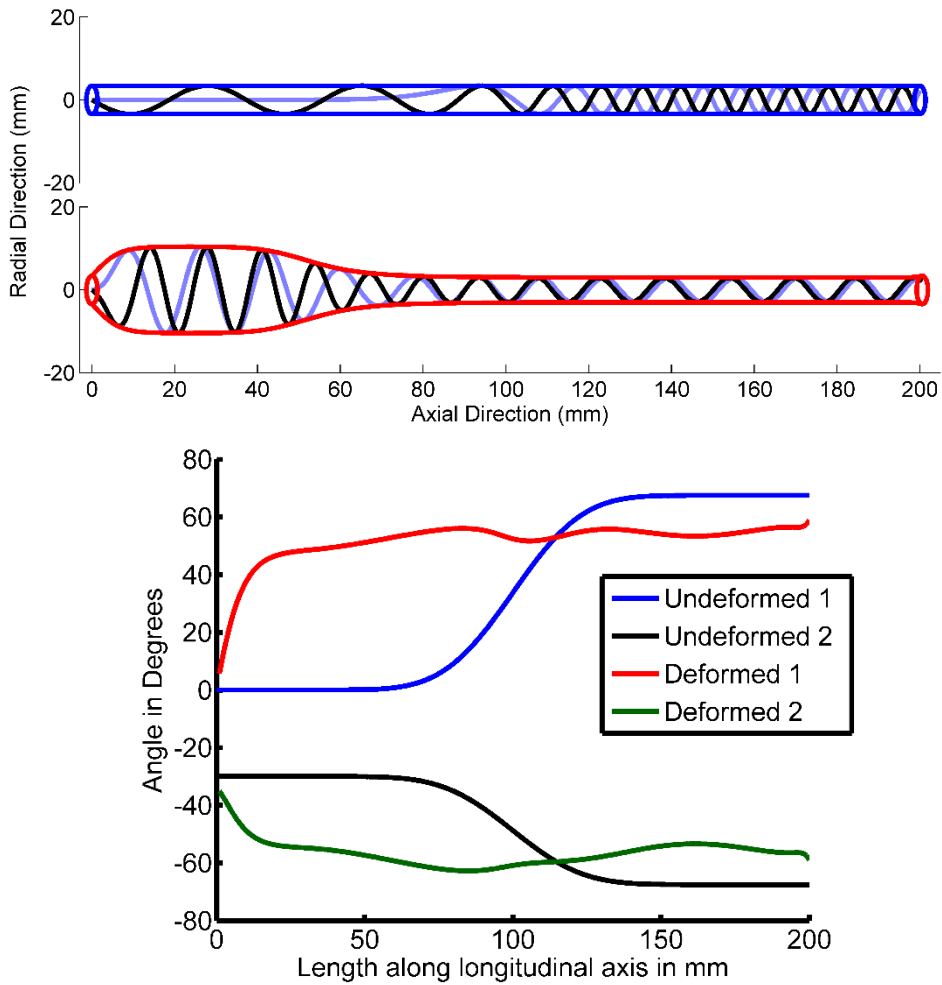
Figure 2-14. (a) Undeformed (top, blue) and deformed (bottom, red) shape of FREE actuator with α varying from $0°$ to $67.5°$ and β varying from $-30°$ to $67.5°$. (b) Variation of fiber angles, α and β along the length of the actuator.

This configuration comprises of a purely extending part that cancels the contraction of the rotating part. The fiber angle variation was chosen purely by trial and error method. One family of fibers varies from $0°$ to $67.5°$ and other family of fibers varies from $-30°$ to $-67.5°$ throughout the length. The actuator was manufactured with length, $L = 200\ mm$, inner radius, $r_0 = 4.76\ mm$ and elastomer thickness, $t = 1.59\ mm$. Actuating over a range of 0 to $0.14\ MPa$, gives a maximum

38

rotation of $220°$ and a maximum change in length of $1.5\,mm$, which is less than 0.5% of its length. Figure 2-15 shows the undeformed and deformed shape of the prototype fabricated, and also compares the deformed profile at $0.14\,MPa$ from the analytical model and experiment. The analytical deformation of this FREE as a function of applied pressure is obtained just as for the rotating FREEs by solving Equation 2.2 subject to Equations 2.3-2.5 with boundary conditions given by Equation 2.13. The material properties of the elastomer were found to be $C_{10} = 0.1716\,MPa$ and $C_{01} = 0.08\,MPa$, similar to the estimation for the McKibben FREEs in Section IV. Figure 2-16 compares the experimental and analytical axial rotation vs. pressure relationship. The slight deviation at higher pressures can be due to the discrepancy between the manufactured and the required fiber angles, especially since they vary long the actuator length. However, it must be noted that simpler models with uniform cylindrical assumptions [5], [6] cannot accurately predict the behavior.
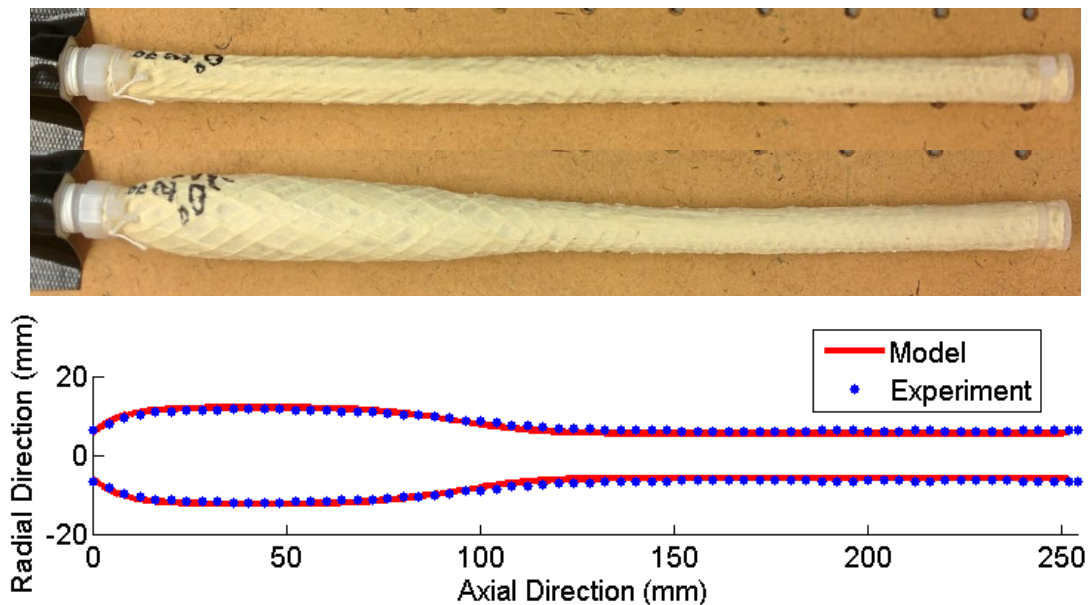
Figure 2-15. Undeformed (top) and deformed (center) shape of purely rotating actuator, and comparison (bottom) with the model.
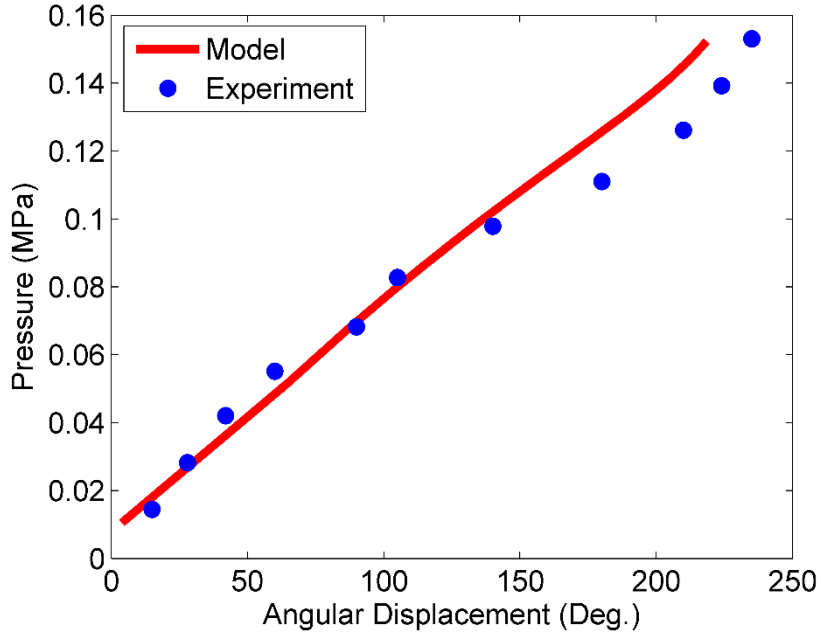
Figure 2-16. Axial rotation comparison for purely rotating FREE.

2.5.2 Varying Material Thickness

Apart from variations in the fiber angle, variations in the elastomer properties can also lead to novel deformations. In this example, we demonstrate a novel PAM that reaches its usual locked deformation profile through unconventional intermediate configurations. In this case, we consider a PAM with constant initial fiber angles: $\alpha = -\beta = 20°$. However, the elastomer thickness for the top half of the actuator is twice the bottom half. The elastomer thickness factors in the strain energy stored given by Equation 2.5. For the same deformation parameters and material properties, the strain energy stored in the elastomer is proportional to its thickness. Thus, upon solving Equation 2.2 subject to Equation 2.14 and 2.5 for various intermediate strain energy values, it is seen that the bottom half deforms first, followed by the top half as shown in Figure 2-17. However, the locked profile (extreme right of Figure 2-17) is a function of kinematics alone.

40
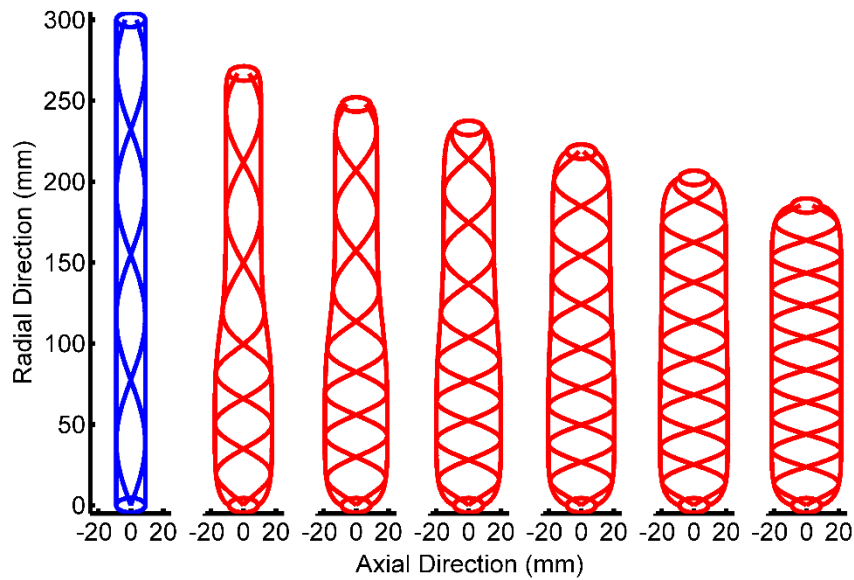
Figure 2-17. Intermediate deformation shapes (red) of a McKibben actuator with variable membrane thickness along the actuator length.

2.6   Conclusions

Fiber Reinforced Elastomeric Enclosures (FREEs) are soft actuators that contract, extend, rotate and provide a combination of these motions upon fluidic actuation. These motion patterns are closely linked with the FREEs reinforced fiber orientations. This chapter presents a generalized and accurate model to predict the deformation profile of FREEs based on a constrained volume maximization approach. The main contributions are:

(a) The ability to capture true curvilinear deformed shape as opposed to uniform cylinder assumption used in literature.

(b) The ability to predict both kinematics and kinetostatic deformation by including the effect of material properties and external load.

41

(c) The ability to predict static behavior of FREEs beyond the popular McKibben pneumatic artificial muscle (PAM), and especially those with asymmetric fibers angles that in general vary along the length of the actuator [14],

(d) The ability to predict realistic deformation profiles by the inclusion of fiber extensibility in the model.

Thus, this paper serves as a bridge between the recent developments in FREE actuators [4] [3] [16], and accurate membrane-based models that are reserved for purely contracting PAMs [7] [8].

The chapter establishes the accuracy and usefulness of the model through extensive experimental validation. First, the model is benchmarked with existing continuum mechanics based models for PAMs where the deformation profiles were observed to match within 10% error. This was followed by experimental validation of in-house McKibben FREEs for their force-deflection relationship. The most important contribution of the paper is in the prediction of the deformation and blocked torque in rotating FREEs (Section V), for which there are no existing literature. The deformed profiles and their relationship with applied pressure match with an error of less than 15%.

3. Soft Pneumatic Sleeve for Arm Orthosis

3.1   Introduction

Patients that use crutches for ambulation experience forces as high as 50% of body weight and extreme extension angles at the wrist, which increases the risk of joint injury such as carpal tunnel syndrome. We have designed and fabricated a soft pneumatic sleeve to reduce the wrist loading by transferring part of the load to the forearm. The sleeve uses a Fiber Reinforced Elastomeric Enclosure (FREE). We have used a contracting FREE, which is wrapped in a helical shape around the forearm as part of the sleeve. Upon actuation, it contracts in length and reduces in diameter, thereby generating a constricting force around the forearm.

(a)   (b)

Figure 3-1. (a) Powered arm orthosis [14]. (b) Lofstrand crutch user during swing-through gait [15].

Current robotic systems mimicking human movement are either heavy and rigid, or flexible and not powerful. While prosthetic devices replace missing body parts, orthotic devices enhance the function of existing body parts. Active orthotic devices are powered and actuate to enhance movement, while passive orthotic devices do not actuate. Active orthoses assist in motion control and joint stability of the user. Of the active orthoses, there has been a focus on lower extremity exoskeletons [16], [17], which is in part due to the quasi-periodic behavior of walking. To generate forces large enough for walking, these devices are also heavy, rigid, and bulky. Movements of the upper extremities tend to be more complex. Simple activities of daily living, such as feeding oneself or hair brushing, can be cumbersome and overbearing for someone with a disability. Powered upper extremity orthoses tend to be mounted to a wheelchair since it is difficult for persons with limited upper extremity ability to wear such heavy and bulky devices (Figure 3-1a). Thus in general, there is a need for lightweight, soft, adaptive and powered orthotic devices for upper extremities.

This chapter focuses on design and analysis of one such upper orthosis for pediatric patients using Lofstrand crutches. In these patients, it is observed that typically close to 50% of their body weight are being transferred on to the wrist in the swing through gate as seen in Figure 3-1b [15], [18], [19]. These unnatural loads placed upon the upper extremity during quadrupedal gait eventually lead to carpal tunnel syndrome, arthritis, or joint deformity [18], [20]–[22]. We have designed a soft pneumatic sleeve as an add-on to a Lofstrand crutch to redirect the load acting on the wrist to the forearm, thereby improving the wrist posture and minimizing the risk for injury. Our design achieves this objective by providing a constriction force about the forearm. This constricting force results in a static friction force around the forearm in the proximal direction.

Furthermore, the sleeve is soft and adaptive and does not restrict the forearm movement (see Figure 3-2).

Figure 3-2. (a) Prototype of pneumatic sleeve, (b) With the user's arm, (c) Demonstrating unrestricted arm movement.

In this chapter, we describe the design and analysis of soft pneumatic sleeve. For analysis, we use the volume maximization approach introduced in Chapter 2 to predict the force generated by FREE actuators upon actuation with pressurized fluids. This will be used to predict the constriction force generated by the soft pneumatic sleeve. This chapter is organized as follows. Section 3.2 describes the design of the sleeve and its manufacturing method. Section 3.3 describes the modeling of sleeve as an active string and predicts the constriction force on the arm from the actuation FREE force. Section 3.4 presents the parametric variation of the performance of the sleeve with respect to geometric variables. Section 3.5 presents initial experimental evaluation of the sleeve system, and comparison with the analysis. Finally, we summarize the contributions and conclude in Section 3.6.

3.2   Design of Pneumatic Sleeve

Soft pneumatic sleeve is designed to be an add-on to a Lofstrand crutch. The primary purpose of the sleeve is to redirect the load acting on the wrist to the forearm, thereby improving the wrist posture and minimizing the risk for injury. At the same time, the sleeve should not restrict the forearm movement. Our design achieves this objective by providing a constriction force about the forearm. This constricting force results in a static friction force around the forearm in the proximal direction.
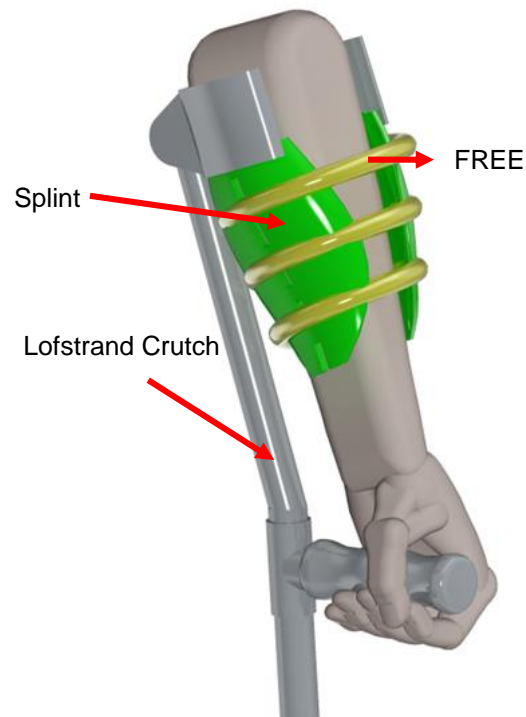

Figure 3-3. Design of the pneumatic sleeve.

The sleeve uses a custom-fabricated FREE to provide the constriction force. FREEs have the following features that make them the most suitable actuators for this application.

a) High power to weight ratio

b) Inherent compliance allowing them to wrap around any contours, which in our case is the forearm of the user.

c) Uses pneumatic actuation which is portable and lightweight.

d) Minimal risks of injury in case of failure.

The sleeve prototype involves two ergonomically designed splints that encase the forearm and are attached to the cuff of the crutch. A FREE actuator which contracts in length and expands radially is wrapped in a helical shape around the outer surface of the splints as shown in Figure 3-3. Both ends of FREE are rigidly attached to the splint and pneumatic actuation is provided to the top end.

FREE actuator is made of a hollow cylindrical tube made of natural rubber latex with inner radius of 4.76 mm and wall thickness of 1.59 mm. Two families of inextensible fibers are wrapped helically on the outer surface of the tube. For pure contraction, which is desired in our application, the two fiber angles should be equal and opposite to each other and should be less than 54.7°. Fiber angles are chosen as $\pm 30°$ for the ease of fabrication.

In the unactuated state, the coiled actuator is in contact with the splint throughout its length. Upon actuation, it reduces in length and increases in diameter. Since, both ends of the actuator are rigidly attached to the splint, it prevents any change in the length and number of coils in the helix, thereby changing only the helical diameter. This change in helical diameter is resisted by the forearm, thereby resulting in a normal force acting on the forearm.

3.3   Analysis of Sleeve

One of the major tasks involved is modeling the constriction force exerted by the helical FREE on the splint attached to cuff and the forearm. The cylindrical shell of the sleeve had an outer diameter of 85.6 mm and height of 99.2 mm. We have developed a reduced order model to simulate the constriction force generated by the FREE as part of the sleeve at different actuation pressures. We are using a FREE that reduces in length and expands radially upon actuation. It is wrapped helically around the forearm with both ends fixed on the sleeve. Therefore, upon actuation when it reduces in length, pitch and number of coils of the helix remain constant allowing a change only in the helical diameter. This change is resisted by the forearm. If we assume the forearm to be perfectly rigid, it applies a normal force on the FREE that prevents this change in diameter. Reaction force acting on the forearm due to this normal force is the constricting force that we are interested in. Since, the forearm prevents any change in helical shape, the tension developed in FREE will be equal to the blocked force, which is the axial force that prevents any change in length for a given actuation pressure.

Due to the negligible bending stiffness of FREE, we can assume that it behaves like a string when it is wrapped helically around the forearm.
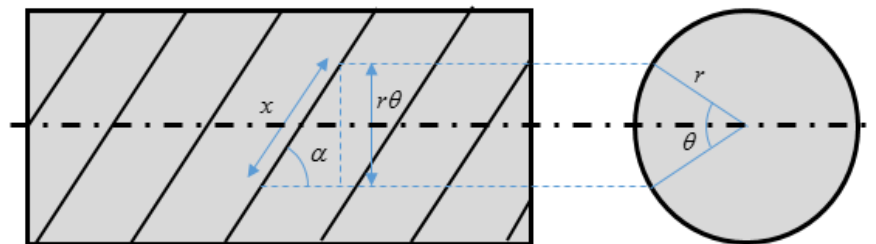

Figure 3-4. FREE wrapped helically around the forearm.

As shown in Figure 3-4, FREE is wrapped helically at angle, α around the forearm to provide the constriction force. For simplicity, the forearm is assumed to be a cylinder with radius, r. Length of an arbitrary section, x is given by

$$x = \frac{r\theta}{\sin\alpha} \tag{3.1}$$
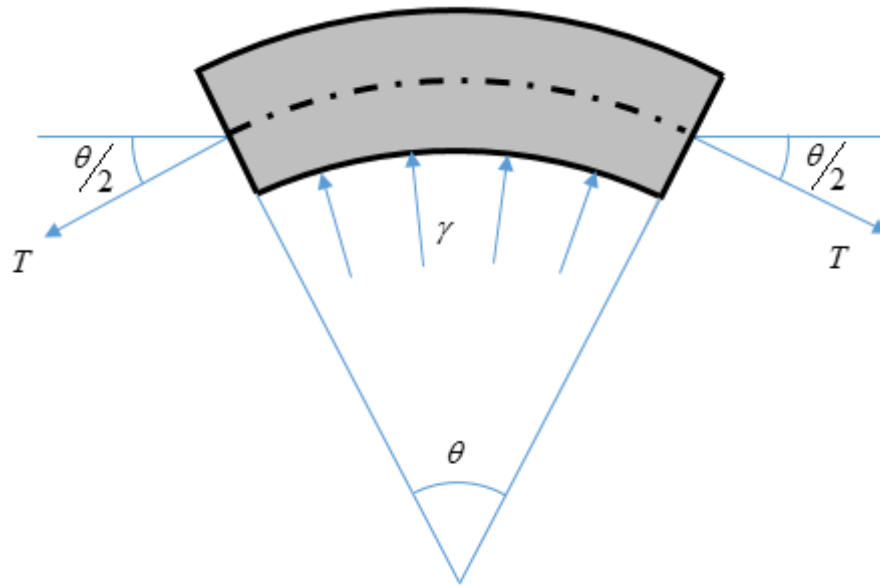
Figure 3-5. Section of coiled FREE showing the normal force and the axial tension.

We consider the free-body diagram of the section, x of the helically coiled FREE. In addition to the axial tension, T acting on both ends of the section, there is a normal force acting along the bottom edge. This normal force represents the constricting force that the FREE applies on the forearm, which is in contact with the bottom edge of the FREE. γ represents the magnitude of this normal force acting per unit length. As we can see in Figure 3-5, due to the symmetry of the section about the y axis, the horizontal component of both T and γ will cancel out resulting in force only in the vertical direction. Vertical resultant of γ is given by

$$F_{normal,y} = \int_x \gamma \cos \varphi \, dx \tag{3.2}$$

Substituting, Equation 3.1 in 3.2 gives,

$$\begin{aligned} F_{normal,y} &= \int_{-\theta/2}^{\theta/2} \frac{\gamma r \cos \varphi}{\sin \alpha} d\varphi \\ &= \frac{2\gamma r \sin \theta/2}{\sin \alpha} \end{aligned} \tag{3.3}$$

Applying force balance in the vertical direction, we can equate the vertical component of T to the vertical component of γ, which upon simplification gives us the following expression,

$$\gamma = \frac{T \sin \alpha}{r} \tag{3.4}$$

Equation 3.4 gives us the relationship between the normal constricting force and the axial tension. Other terms in Equation 3.4 can be obtained from the geometry of the helix.

3.4 Parametric Analysis of FREEs

Primary purpose of the sleeve is to provide the constricting force around the forearm, γ. In order to design a FREE that generates the desired γ, its variation with respect to the design parameters need to be studied. As shown in Equation 3.4, γ depends on the blocked force, helix angle and radius of the coil. Blocked force is obtained by solving the maximization problem given by Equation 2.2 subjected to Equations 2.5, 2.6, and 2.14, where the constraint is equated to the undeformed length of FREE. Therefore, we do not have an explicit expression showing the

variation of blocked force with respect to the design parameters namely radius, length, and fiber angle of the FREE. We have done a parametric study that shows these variations by varying one of the parameters while keeping others fixed.

Carrying out the analysis of FREE while keeping all the other dimensions constant and varying only the fiber angle at three different actuation pressures gives the plot shown in Figure 3-6. As we can see from Figure 3-6, blocked force reduces exponentially with increasing fiber angle and becomes zero at $54.7°$, which is one of locked configurations of FREEs.

Similarly, Figure 3-7 and Figure 3-8 show the variation of blocked force with change in length and radius of FREE, respectively while all the other dimensions are kept constant. From Figure 3-7, we can see that blocked force is independent of the actuator length. On the other hand, Figure 3-8 shows that the blocked force increases with increase in actuator radius.

Based on the force requirements and dimension of the sleeve, we choose a FREE with fiber angle of $30°$, length of 640mm, inner radius of 4.76 mm and wall thickness of 1.59mm for the elastomeric tube.
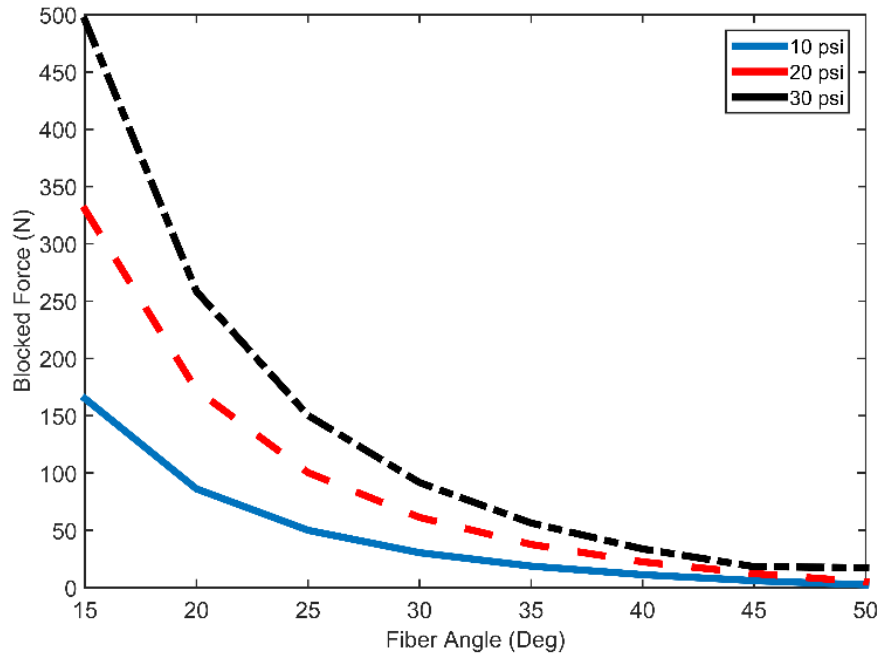
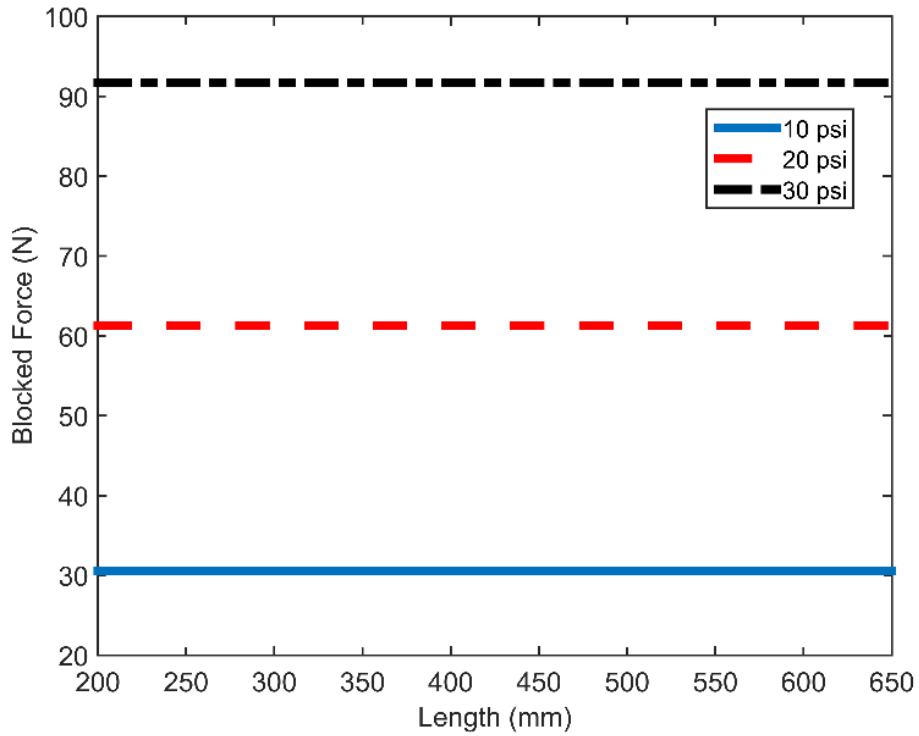Figure 3-6. Variation of blocked force with fiber angles.

Figure 3-7. Variation of blocked force with actuator length.
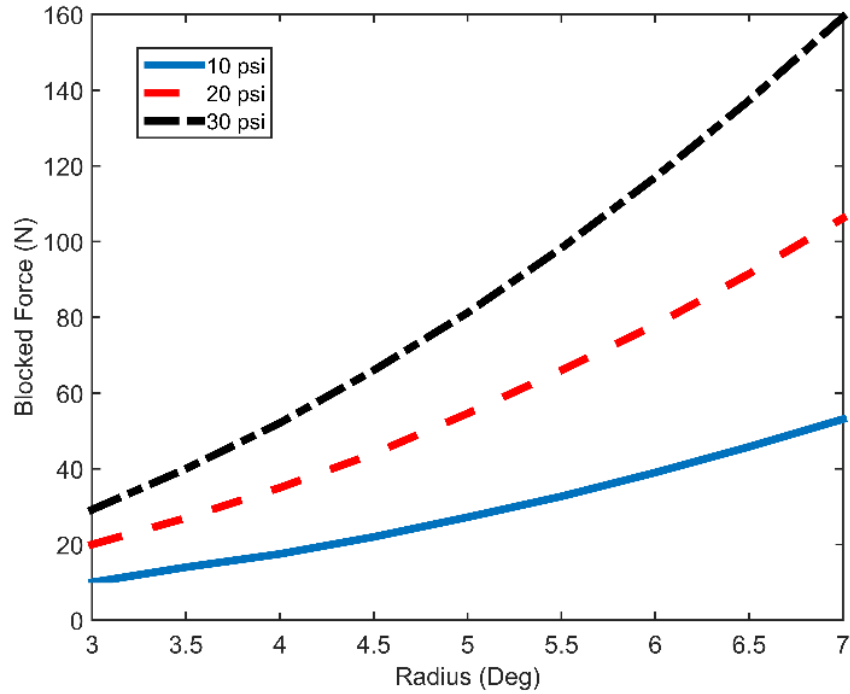
Figure 3-8. Variation of blocked force with actuator radius.

3.5 Experiments

To validate our FREE analysis model, we carried out two experiments. In the first one, we applied actuation pressure ranging from 5 psi to 30 psi and measured the length of the FREE. Figure 3-9 shows that the experimental data matches well with the analytical model with less than 10% maximum error.

In the second experiment, we measured the blocked force generated by FREE at different actuation pressure. The experimental setup is shown in Figure 3-10. One end of the FREE is used for actuation and the other end is connected to a load cell, which measures the force required to prevent any change in length of FREE at different pressure. The plot shown in Figure 3-11 shows

an offset error between experimental and analysis data. This discrepancy can be attributed to the small amount of extension in the fibers, which can be corrected by introducing 0.75% of extension in the fibers. After introducing extensibility of fibers in the analysis, it matches closely to the experimental data with maximum error of 10%

To validate the string model that estimates the constricting force, we conducted an experiment for which the setup is shown in Figure 3-12. The experimental setup consists of two 3D-printed halves of a cylindrical shell, which are placed around an air bladder. FREE is wrapped helically around the outer surface of the shell. First, the FREE is actuated followed by pressurization of the air bladder till the point when the shells separate. Then the pressure in the bladder is released till the shells come in contact. The corresponding bladder pressure is taken as the normal pressure generated by the FREE and can be converted to normal force per unit length of FREE.

Comparison of normal force generated by FREE is shown in Figure 3-13. We used the string model described in Section 4 with blocked force values obtained both experimentally and using our analytical model. There is almost 50% error in the force predicted by string model compared to the experimentally observed constriction force. Upon further investigation, we observed a decrease in the blocked force generated by FREE, when there is normal force acting along its length. This decrease causes the error between our predicted and experimental constriction forces shown in Figure 3-13, because there will be a decrease in the blocked force due to the constriction force acting along the length of FREE when it is wrapped around the splint as shown in Figure 3-12.
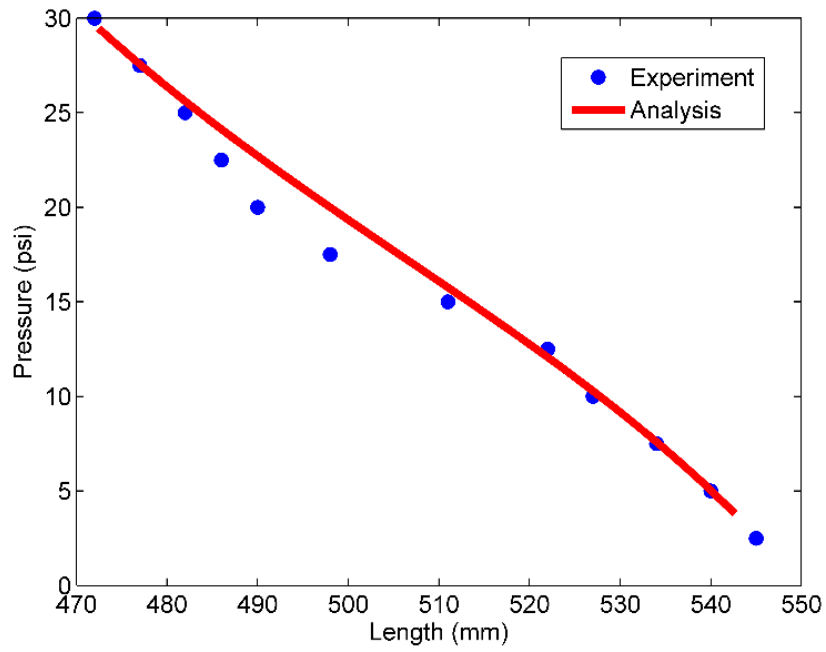
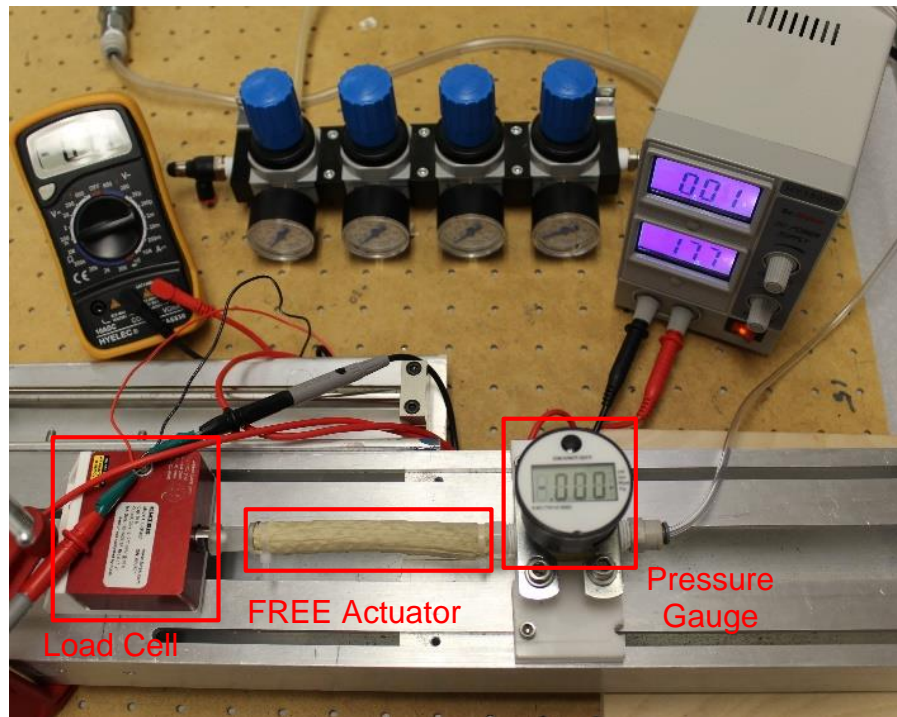Figure 3-9. Actuation pressure vs. length of FREE.

Figure 3-10. Experimental setup for blocked force measurement.
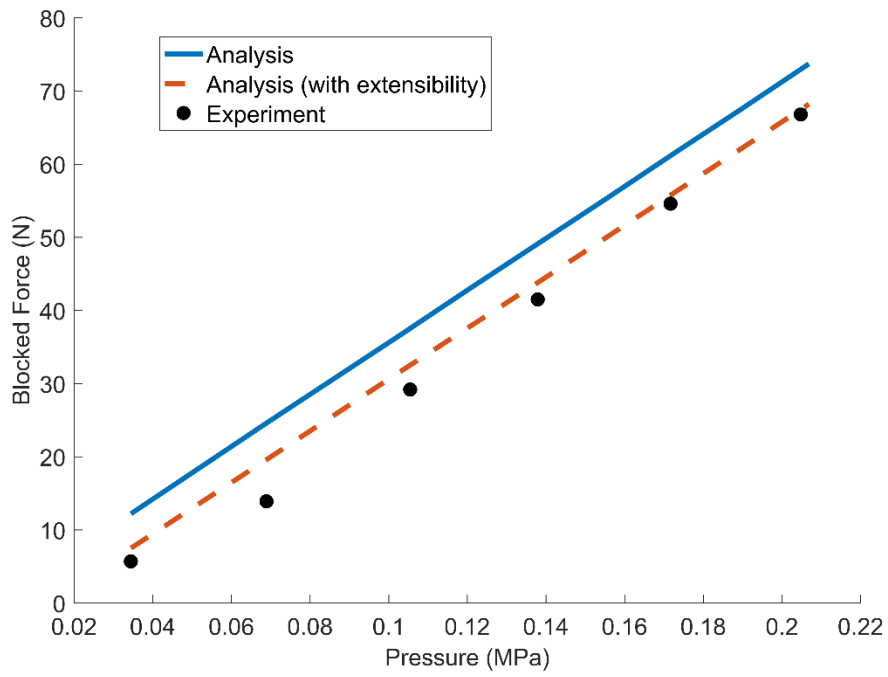
Figure 3-11. Blocked force vs. actuation pressure.

Figure 3-12. Experimental setup to measure the constricting force generated by the sleeve.
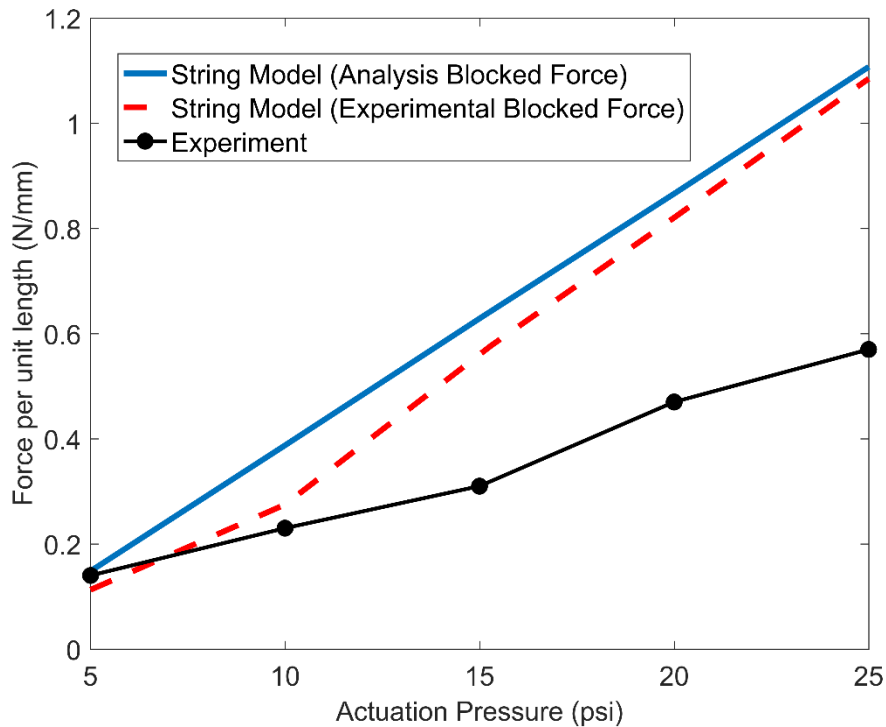
Figure 3-13. Normal force per unit length of FREE vs. actuation pressure.

3.6   Conclusions and Discussion

3.6.1 Discussion

Comparison between analytical and experimental blocked force shows that the constrained volume maximization formulation described in Chapter 2 can predict the blocked force accurately. On the other hand, there is a significant deviation between analytical and experimental constriction force per unit length, where the analytical force is obtained by using the string model and using the blocked forces obtained both analytically and experimentally. On further investigation, it was found that the blocked force decreases when there is a normal force acting along the length of FREE in the form of constriction force. Our next step would be to model this decrease in blocked

force, so that we can have a model that can accurately predict the constriction force generated by the soft pneumatic sleeve.

3.6.2 Conclusion

We have designed a soft pneumatic sleeve orthosis for crutch users to improve the wrist posture and redirect partial load from wrist to forearm. The sleeve uses a helically coiled FREE that contracts in length and expands radially upon actuation, thereby generating a constricting force around the forearm. We have used a constrained volume maximization approach to model the blocked force generated by the FREE. This blocked force is then related to the constricting force using a string model. A parametric analysis on blocked force is carried out to aid in the design process. The model is validated by comparing with experimental results.

4. Conclusions and Future Work

4.1 Conclusions

Fiber Reinforce Elastomeric Enclosures (FREEs) are soft and flexible actuators made of hyperelastic membrane and inextensible fibers. FREEs can generate different motion patterns that include extension, contraction, rotation, and a combination of these motions. The commonly used Pneumatic Artificial Muscles (PAM) [3], [4] are a special case of FREEs where the two families of fiber angles are equal and opposite. PAMs are commonly used in robotics, and aerospace applications. FREEs being a more generalized form of PAMs are suitable for these applications and can also find applications in human-assistive devices, pipe inspections, wearable robots, etc. To design such devices, there is a need for a simple and accurate model to describe the deformation behavior of FREEs. The current models in literature have the disadvantage of being applicable only to the special case of PAMs or being computationally too intensive or using involving simplifying assumptions. This thesis proposes a generalized energy based model to predict the deformation behavior of FREEs by posing a constrained volume maximization problem. The model is based on the observation that inflatable objects tend to maximize their enclosed volume while conforming to certain physical constraints. In the case of FREEs, these physical constraints are due the inextensibility of fibers and energy stored in the hyperelastic membrane. The model has the added advantage of decoupling kinematics and kinetostatics, thereby making it computationally less intensive. The model captures the curvilinear deformed shape of FREEs, kinematics due to wrapped fibers, and kinetostatics due to the hyperelastic membrane. It can predict the actuation pressure versus stroke length and rotation as well as the force-deflection and

59

torque-rotation relationship for any FREE at any given actuation pressure. Therefore, this model can be used to predict the complete static deformation behavior of any FREE.

Accuracy of the model is ascertained by benchmarking with existing continuum mechanics based models of PAMs, where the deformation profiles were matched with less than 10% error. In addition, extensive experiments were carried out over six different prototypes of FREEs. These experiments showed that the model accurately captures the static deformation behavior of FREEs. It is also shown that the model can take into account variations in fiber angles and membrane thickness. None of the models available in literature can account for these variations.

In Chapter 3, design of a soft pneumatic sleeve orthosis is demonstrated that uses a FREE to provide constriction force around the forearm of a Lofstrand crutch user. Motivation for the design comes from studies [15], [18] that have shown that patients using Lofstrand crutches experience close to 50% of body weight at the wrist joint, which can lead to wrist injuries, carpal tunnel syndrome, and joint deformity. It is shown that FREEs due to their high power to weight ratio, compliance, and minimal risk of injury threat to user are appropriate choice of actuation for human assistive devices. The analysis model developed in Chapter 2 is used to obtain the axial force generated by FREE. This is then combined with a string model introduced in chapter 3 to analyze the constriction force applied by sleeve on forearm of crutch user. Experiments are carried out to compare the model with experimentally observed forces.

4.2 Future Work

For controls and system-level implementation, there is a need for a dynamics model for FREEs. Therefore, one line of future work can involve extending the model to incorporate dynamic characteristics and also to study hysteresis.

FREEs being soft actuators, generate force and moment. Therefore, they can be used to replace rotary motors and linear actuators. With the analysis model developed in Chapter 2, graphs describing force-deflection and torque-rotation relationships can be developed for any FREE for given fiber angles, length, and radius of hyperelastic membrane. A possible extension of this model would be to extend the formulation to develop a design framework which can solve the inverse problem, where for any given kinematic or kinetostatics behavior such as force-deflection or torque-rotation data, the design tool determines the fiber angles, length, and radius of FREE that can generate those behavior upon actuation. Furthermore, the framework can be used to design novel FREEs with arbitrary varying fiber angles and membrane properties similar to the ones shown in Chapter 2. This approach of analysis could also be generalized such that it can be used to analyze any inflatable rubber-like cavities with arbitrary shapes that can find use in the field of soft robotics.

References

[1]   D. Trivedi, C. D. Rahn, W. M. Kier, and I. D. Walker, "Soft robotics: Biological inspiration, state of the art, and future research," *Appl. Bionics Biomech.*, vol. 5, no. October 2015, pp. 99–117, 2008.

[2]   C. Majidi, "Soft Robotics: A Perspective—Current Trends and Prospects for the Future," *Soft Robot.*, vol. 1, no. 1, pp. 5–11, 2014.

[3]   Y. Shan, M. P. Philen, C. E. Bakis, K. W. Wang, and C. D. Rahn, "Nonlinear-elastic finite axisymmetric deformation of flexible matrix composite membranes under internal pressure and axial force," *Compos. Sci. Technol.*, vol. 66, pp. 3053–3063, 2006.

[4]   W. Liu and C. R. Rahn, "Fiber-Reinforced Membrane Models of McKibben Actuators," *J. Appl. Mech.*, vol. 70, no. November 2003, p. 853, 2003.

[5]   G. Krishnan, J. Bishop-Moser, C. Kim, and S. Kota, "Kinematics of a Generalized Class of Pneumatic Artificial Muscles," *J. Mech. Robot.*, vol. 7, pp. 41014-1–9, 2015.

[6]   J. Bishop-Moser and S. Kota, "Design and Modeling of Generalized Fiber-Reinforced Pneumatic Soft Actuators," *IEEE Trans. Robot.*, vol. 31, no. 3, pp. 536–545, 2015.

[7]   C. S. Kothera, M. Jangid, J. Sirohi, and N. M. Wereley, "Experimental Characterization and Static Modeling of McKibben Actuators," *J. Mech. Des.*, vol. 131, no. September 2009, p. 91010, 2009.

[8]   F. Connolly, P. Polygerinos, C. J. Walsh, and K. Bertoldi, "Mechanical Programming of Soft Actuators by Varying Fiber Angle," *Soft Robot.*, vol. 2, no. 1, pp. 26–32, 2015.

[9]   W. H. Paulsen, "What Is the Shape of a Mylar Balloon ?," *Am. Math. Mon.*, vol. 101, no. 10, pp. 953–958, 1994.

[10] R. E. Kalaba and K. Spingarn, "Optimization of functionals subject to integral constraints," *J. Optim. Theory Appl.*, vol. 24, no. 2, pp. 325–335, 1978.

[11] W. H. Paulsen, "What Is the Shape of a Mylar Balloon ? Author (s): William H . Paulsen Source : The American Mathematical Monthly , Vol . 101 , No . 10 (Dec ., 1994), pp . 953-958 Published by : Mathematical Association of America Stable URL : http://www.jstor.org/st," vol. 101, no. 10, pp. 953–958, 2009.

[12] R. Weinstock, *Calculus of variations: with applications to physics and engineering*. Courier Corporation, 1952.

[13] G. Singh and G. Krishnan, "An Isoperimetric Formulation to predict Deformation Behavior of Pneumatic Fiber Reinforced Elastomeric Actuators," in *IEEE/RSJ International Conference on Intelligent Robots and Systems*, 2015, pp. 1738–1743.

[14] J. L. Herder, N. Vrijlandt, T. Antonides, M. Cloosterman, and P. L. Mastenbroek, "Principle and design of a mobile arm support for people with muscular weakness.," *J. Rehabil. Res. Dev.*, vol. 43, no. 5, pp. 591–604, 2006.

[15] B. a. Slavens, P. F. Sturm, R. Bajournaite, and G. F. Harris, "Upper extremity dynamics during Lofstrand crutch-assisted gait in children with myelomeningocele," *Gait Posture*, vol. 30, pp. 511–517, 2009.

[16] A. Dollar and H. Herr, "Lower Extremity Exoskeletons and Active Orthoses:Challenges and State-of-the-Art," *IEEE Trans. Robot.*, vol. 24, no. 1, pp. 144–158, 2008.

[17] K. A. Shorter, G. F. Kogler, E. Loth, W. K. Durfee, and E. T. Hsiao-Wecksler, "A portable powered ankle-foot orthosis for rehabilitation.," *J. Rehabil. Res. Dev.*, vol. 48, no. 4, pp. 459–472, 2011.

[18] B. a. Slavens, P. F. Sturm, and G. F. Harris, "Upper extremity inverse dynamics model for crutch-assisted gait assessment," *J. Biomech.*, vol. 43, no. 10, pp. 2026–2031, 2010.

[19] K. a Konop, K. M. B. Strifling, M. Wang, K. Cao, J. P. Schwab, D. Eastwood, S. Jackson, J. D. Ackman, and G. F. Harris, "A biomechanical analysis of upper extremity kinetics in children with cerebral palsy using anterior and posterior walkers.," *Gait Posture*, vol. 30, pp. 364–369, 2009.

[20] J. L. Mercer, M. Boninger, A. Koontz, D. Ren, T. Dyson-Hudson, and R. Cooper, "Shoulder joint kinetics and pathology in manual wheelchair users," *Clin. Biomech.*, vol. 21, pp. 781–789, 2006.

[21] I. H. Sie, R. L. Waters, R. H. Adkins, and H. Gellman, "Upper extremity pain in the postrehabilitation spinal cord injured patient.," *Arch. Phys. Med. Rehabil.*, vol. 73, pp. 44–48, 1992.

[22] S. Lal, "Premature degenerative shoulder changes in spinal cord injury patients," *Spinal Cord*, vol. 36, pp. 186–189, 1998.